Supporting Information for:

Bulk and nanocrystalline cesium lead halide perovskites as seen by halide magnetic resonance

Laura Piveteau,[†,‡,⊥] Marcel Aebli,[†,‡] Nuri Yazdani,[∥,¥] Marthe Millen,[†] Lukas Korosec,[§,¶] Franziska Krieg,[†,‡] Bogdan M. Benin,[†,‡] Viktoriia Morad,[†,‡] Christophe Piveteau,[§] Toni Shiroka,[§,#] Aleix Comas-Vives,[†,⊥] Christophe Copéret,[†] Aaron M. Lindenberg,[¥,$] Vanessa Wood,[∥] René Verel[†] and Maksym V. Kovalenko*[†,‡]*

[†]Department of Chemistry and Applied Biosciences, ETH Zürich, Vladimir Prelog Weg 1-5, CH-8093, Switzerland

[‡]Empa-Swiss Federal Laboratories for Materials Science and Technology, Dübendorf, Überlandstrasse 129, CH-8600, Switzerland

[§]Department of Physics, ETH Zürich, Otto Stern Weg 1, CH-8093, Switzerland

[#]Paul Scherrer Institute, Villigen PSI, CH-5232, Switzerland

[∥]Department of Information Technology and Electrical Engineering, ETH Zürich, CH-8092, Switzerland

[¥]Department of Materials Science and Engineering, Stanford University, Stanford, California 94305, United States

$Institute for Materials and Energy Sciences, SLAC National Accelerator Laboratory, Menlo Park, California, 94025, United States

Present addresses

⊥L. Piveteau: CNRS, UPR 3079, CEMHTI, 45071 Orléans Cedex 02, France

¶L. Korosec: Department of Quantum Matter Physics, University of Geneva, 24 Quai Ernest-Ansermet, CH-1211, Switzerland

ǂA. Comas-Vives: Departament de Química, Universitat Autònoma de Barcelona, Cerdanyola del Vallès 08193 Bellaterra, Catalonia, Spain

Table of Contents

Supplementary Note S1. Crystal structures of lead-halide perovskites

The cubic perovskite structure is the high-temperature phase for almost all $APbX_3$ compounds.[1-4] However, at room temperature (RT), this highest symmetry structure is stable only for $MAPbCl_3$ (MA = $CH_3NH_3^+$, methylammonium),[2] $MAPbBr_3$,[2] and $FAPbBr_3$ (FA = $CH(NH_2)_2^+$, formamidnium),[5] whereas other $APbX_3$ compositions adopt tetragonal (I4/mcm for $MAPbI_3$),[2] orthorhombic (Pbnm for $CsPbBr_3$)[6] or monoclinic ($P2_1/m$ for $CsPbCl_3$)[7] perovskite polymorphs (Figure 2), which can be derived from the cubic perovskite lattice *via* tilting of the PbX_6 octahedra. Exceptions are $FAPbI_3$ and $CsPbI_3$, which at ambient conditions lose corner-sharing topology and respectively adopt face- and edge-sharing 1D-network structures as their thermodynamically stable phases.[8-9] A summary of the phase transitions and crystal structures of all perovskite $APbX_3$ phases is provided in the Supplementary Table S1.

Supplementary Table S1. Space groups and phase transition temperatures for $APbX_3$ (A = Cs, MA, FA; X = Cl, Br, I) perovskites and perovskite related materials

A-cation	Halide X	composition	Dimensionality	Space group	Stable temp.	Source
Cs	Cl	$CsPbCl_3$	3D	$Pm\bar{3}m$	> 320 K	ref.[1, 6-7]
			3D	$P4/mbm$	315-320 K	
			3D	$Cmcm$	310-315 K	
			3D	$P2_1/m$	< 310 K	
	Br	$CsPbBr_3$	3D	$Pm\bar{3}m$	>403 K	ref.[6 1]
			3D	$P4/mbm$	361-403 K	
			3D	$Pbnm$	< 361 K	
	I	$CsPbI_3$	3D	$Pm\bar{3}m$	> 554-602 K	ref.[1, 8, 10-11]
			3D	$P4/mbm$	457-554 K	
			3D	$Pbnm$	<457 K	
			1D	$Pnma$	< 553-602 K	
MA	Cl	$MAPbCl_3$	3D	$Pm\bar{3}m$	> 177 K	ref.[2, 12]
			3D	$P4/mmm$	172-177 K	
			3D	$Pnma$ / $P222_1$	< 172 K	
	Br	$MAPbBr_3$	3D	$Pm\bar{3}m$	> 237 K	ref.[13]
			3D	$I4/mcm$	155-237 K	
			3D	$P4/mmm$	150-155 K	
			3D	$Pna2_1$	< 145 K	
	I	$MAPbI_3$	3D	$Pm\bar{3}m$	> 330 K	ref.[14]
			3D	$I4/mcm$	162-330 K	
			3D	$P4/mbm$	< 162 K	
FA	Br	$FAPbBr_3$	3D	$Pm\bar{3}m$	> 270 K	ref.[5, 15]
			3D	$P/4mbm$	140-270 K	
			3D	$Pnma$	< 140 K	
	I	$FAPbI_3$	3D	$Pm\bar{3}m$	> 406 K	ref.[3, 16]
			1D	$P6_3/mmc$	<406 K	

Supplementary Table S2. NMR properties of quadrupolar halide nuclei

Nucleus	Spin[17]	Natural Abundance[17]	Gyromagnetic Ratio γ (10^6 rad s^{-1} T^{-1})[17]	Quadrupole moment Q ($e \cdot fm^{-2}$)* [17]
^{35}Cl	$^3/_2$	75.76%	26.241991	-8.165
^{37}Cl	$^3/_2$	24.24%	21.843688	-6.435
^{79}Br	$^3/_2$	50.69%	67.25619	30.5
^{81}Br	$^3/_2$	49.31%	72.49779	25.4
^{127}I	$^5/_2$	100%	53.8957	-71

* e stands for the elementary charge $1.602 \cdot 10^{-19}$ C, with which the tabulated value Q must be multiplied in order to obtain the quadrupole moment in C/fm^2.

Supplementary Note S2. NMR and NQR spectroscopy of halide nuclei

Basic introduction and comparison of NMR and NQR

Solid-state nuclear magnetic resonance (NMR) and nuclear quadrupole resonance (NQR) are two complementary magnetic resonance methods.[18-20] They are versatile, non-perturbing analytical methods, which are sensitive to structural properties and the chemical surrounding of an atomic nucleus, as well as to dynamic processes. Both capture the effects of the quadrupole interaction, which is the interaction between the electric field gradient (EFG) and the quadrupole moment of a nucleus. The EFG is described by a tensor of rank two and is parametrized by the asymmetry (η_Q) and the coupling strength given by the quadrupole constant (C_Q). It is produced by neighboring nuclei and electrons and reflects the chemical and electronic surrounding of a spin.

In NMR spectroscopy, the Zeeman interaction (H_{ZE}) induces the splitting of the nuclear spin states in a magnetic field. The spin energy transitions scale with the magnetic field strength and are characterized by the Larmor frequency, ω_0. Slight deviations therefrom are induced by perturbing interactions such as the chemical shift or the dipole-dipole coupling.

For small quadrupole interactions, a perturbation approach is convenient to describe the spin system.[21-22] If, instead, the Larmor frequency is of similar size as C_Q, the perturbation approximation breaks down and an exact calculation of the spectral features is required to interpret the NMR spectra of quadrupolar nuclei.[23] In such case, the NMR signals are very broad (several MHz in width) and the line-narrowing approaches which are commonly used in NMR spectroscopy, such as the rotation of the sample around the magic angle (magic angle spinning, MAS), do not bring imrpovements. It is therefore not surprising that the acquisition of halide NMR spectra of lead-halide perovskites materials has so far proven to be very challenging. A detailed discussion of the quadrupole interaction is found in the Supplementary Notes S3.

In the case of very large quadrupole interactions, in the range of several tens to hundreds of MHz, omitting the Zeeman interaction facilitates the study of spin energy transitions. Detection of NQR is conceptually the same as that of NMR, except that it does not require an external magnetic field. In pure NQR, only the EFG will lead to spin energy splitting in the form of the quadrupole interaction. In the case of half-integer quadrupolar spins, the EFG does not lift the degeneracy between spin states with magnetic quantum numbers $\pm m_I$, as illustrated with the example of a spin $I = {}^3/_2$ in Supplementary Figure S1. The greatest limitation of NQR spectroscopy is the difficulty to find the resonance lines, as there are no isotope-specific frequency regions. Depending on the size of the quadrupole interaction, the signals can appear between a few Hz and several hundreds of MHz. Without a sufficiently accurate prior guess, *e.g.* from quadrupole parameters extracted from NMR spectra or from DFT calculations, finding NQR frequencies resembles searching for a needle in a haystack. Once the resonance frequencies are known, recording the signal becomes relatively straightforward. In pure NQR spectra, the line widths are often narrow and are easily recorded with simple one-pulse or Hahn echo experiments. For strong quadrupole interactions, the

large spin energy difference results in large population differences, described by Boltzmann statistics, which is equivalent to more intense signals. Hence, in NQR, it is not possible to correlate the signal intensity to spin concentrations in the sample, especially when the resonance frequencies of the compared signals are far apart. In the case of a spin $I = {}^3/_2$, NQR suffers from an additional drawback: only one NQR transition is allowed ($m_Q = \pm{}^1/_2 \rightarrow m_Q = \pm{}^3/_2$), and this is insufficient to determine the two quadrupole parameters, C_Q and η_Q, which define the EFG tensor and thereby the chemical surrounding of the spin. For quadrupolar spins $I \neq {}^3/_2$, C_Q and η_Q can be deduced from the sufficiently large number (≥ 2) of NQR transitions.

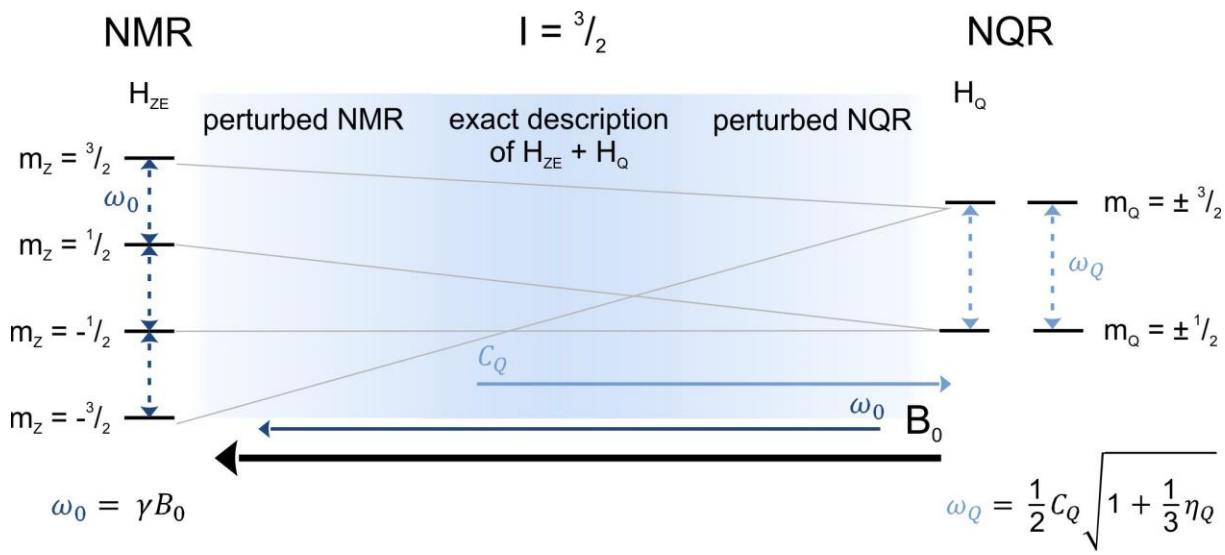

Supplementary Figure S1 | Scheme of the continuous transition from NMR to NQR. In pure NMR, only the Zeeman interaction (H_{ZE}) leads to spin energy splitting, whereas in pure NQR, only the quadrupolar interaction (H_Q) leads to spin energy splitting. The transition from one to the other occurs when the applied magnetic field strength (B_0) decreases, and with it the Larmor frequency (ω_0) or the quadrupole coupling constant (C_Q) increase.[19] The example of a spin $I = {}^3/_2$ is used to illustrate the fate of the spin states when transforming from the Zeeman frame ($m_Z = {}^3/_2, {}^1/_2, -{}^1/_2, -{}^3/_2$) to the principle axes of the quadrupole ($m_Q = {}^3/_2, {}^1/_2$). In the absence of other interactions, the spin energy transitions of the two extreme cases are well described by the Larmor frequency or by the quadrupole frequency (ω_Q), respectively. If either the Zeeman or the quadrupole interaction dominates, NMR and NQR spectra can be appropriately described using the perturbation approach. In the intermediate regime, where the C_Q is of comparable value as ω_0, an exact description of the nuclear spin system is required.

There is no fixed ratio between C_Q and ω_0 at which perturbation approaches fail or at which NQR becomes a more appropriate analytical technique than NMR. Instead, there exists a continuum between the two situations, from when the spin states are defined exclusively by the Zeeman interaction (left side of Supplementary Figure S1) to when the EFG is solely responsible for the

spin energy splitting (Supplementary Figure S1). The smooth transition from an NMR to an NQR experimental regime is driven by the increase of the quadrupole interaction strength given by C_Q and/or the reduction of the external magnetic field strength B_0, which is equivalent to a reduction of the Larmor frequency, ω_0. NQR is favored over NMR in case of large C_Q (several tens to hundreds of MHz). NQR and NMR signals are induced or influenced by the quadrupole interaction and both contain information about the strength, the symmetry and the fluctuation of the EFG and hence about the electrons and nuclei around a spin. For structural information, the line shape analysis in NMR and the frequency analysis in NQR provide all the required information from the evaluation of C_Q and η_Q. C_Q corresponds to the strength of the coupling, which encodes the distance of the charges relative to the spin, and η_Q describes the symmetry of the EFG and the arrangement of the charges in the spin surrounding.

Halide NMR and NQR

Producing sufficiently strong static external magnetic fields for the Zeeman interaction to dominate over the quadrupole interaction of halide nuclear spins is technically limited. Consequently, the magnetic resonance studies on $^{35/37}$Cl, $^{79/81}$Br and ^{127}I spins in lead-halide perovskite materials have thus far focused on NQR.[24-32] ^{35}Cl,$^{79/81}$Br and ^{127}I NQR helped to elucidate the symmetry of the nuclei's surroundings and the phase transitions in $CsPbCl_3$,[24-26] $MAPbCl_3$,[27] $CsPbBr_3$,[28-29] $MAPbBr_3$,[27] $CsPbI_3$,[29] $MAPbI_3$.[27, 30-33] and $FAPbI_3$.[33]

In this work, we present the first ^{35}Cl and ^{79}Br NMR spectra of $CsPbCl_3$ (bulk and NCs, Fig. 3 and Supplementary Fig. S2) and $CsPbBr_3$ (bulk, Fig. 5), as well as $MAPbBr_3$ and $FAPbBr_3$ (both bulk, Supplementary Fig. S3). The acquisition of sub-spectra (3 for $CsPbCl_3$ and 42 for $CsPbBr_3$) and the possibility to refocus the magnetization by Carr-Purcell-Meiboom-Gill (CPMG) pulse trains, both indicate that the halide NMR signals are inhomogeneously broadened. The ^{35}Cl NQR spectra were not recorded, due to the low resonance frequencies expected around 7.7 MHz (as calculated from the quadrupole parameters obtained from the NMR spectra and as reported in literature).[24] Their intensities are low because of the Faraday's law of induction and unfavorable Boltzmann statistics for such small energy transitions. The larger quadrupole couplings of lead-bromide perovskites (133.59, 136.36 MHz for $CsPbBr_3$, 141.02 MHz for $MAPbBr_3$ and 149.10 MHz for $FAPbBr_3$) allow for a more facile recording of their NQR spectra. The ^{79}Br NQR spectrum of bulk $CsPbBr_3$ consists of two lines, one line per bromine species (one for the two axial bromines at lower frequencies and one for the four equatorial bromines at higher frequencies, see Figure 5b). Equivalent ^{81}Br NQR lines are found at lower frequencies[28-29] and provide the same information about the EFG at bromine sites as ^{79}Br NQR transitions. For $CsPbBr_3$ NCs, no signal was found at lower frequencies, where the second signals from orthorhombic and tetragonal crystal structures are expected although the spectral range down to -76.66 MHz was screened. Since the NC signal (Figure 5b) exhibits strong inhomogeneous broadening, a comparable effect must also apply to the low-frequency line of eventual orthorhombic and tetragonal phases. However, its effective width

is probably broader as the inhomogeneous broadening scales with the absolute resonance frequency. Hence, the signal might be too broad and too weak to be resolved from noise.

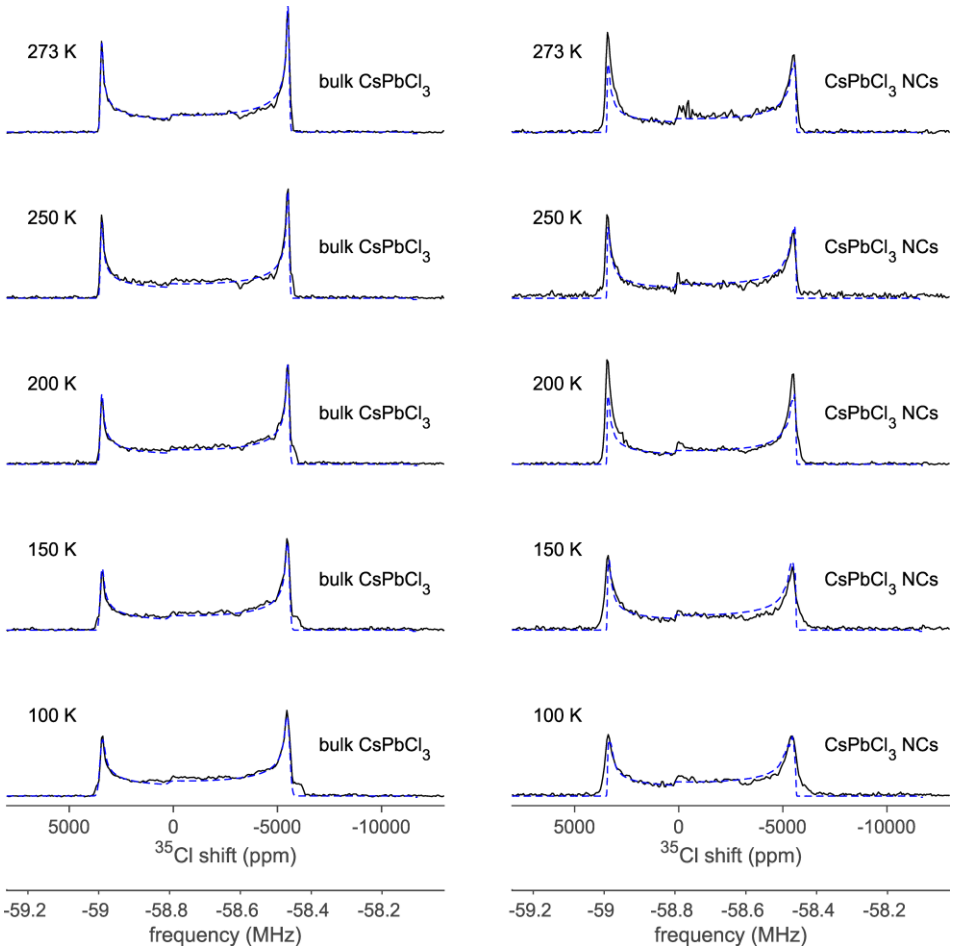

Supplementary Figure S2 | ^{35}Cl NMR static spectra of bulk $CsPbCl_3$ and $CsPbCl_3$ NCs recorded at various temperatures. The experimental data is plotted as black, solid lines. The signals are constructed by taking the skyline of three wide-band, uniform-rate, and smooth truncation - Carr-Purcell-Meiboom-Gill (WURST-CPMG) sub-spectra with different frequency offsets for each temperature. The simulations (blue, dashed lines) are based on the exact description of the quadrupole interaction in the Zeeman frame. Other spin interactions and the chemical shift anisotropy (CSA) could be neglected due to their low influence on the spectra (Supplementary Fig. S4). All bulk $CsPbCl_3$ could be simulated with C_Q = 15.48 MHz, η_Q = 0, δ_{iso} = 221 ppm and only small variations of the amplitude were required to match the experimental data due to increasing Gaussian line broadening for lower temperatures. The $CsPbCl_3$ NCs spectra could be simulated with C_Q = 15.51 MHz, η_Q = 0, δ_{iso} = 221 ppm, except for the one at 100 K, where C_Q= 15.49 MHz was used. The Gaussian broadening was kept constant for all simulations of NC spectra, but Maurer statistics[34] was included by implementing the analytical joint distribution density reported by Seleznyova *et al.*[35] to account for the distribution of quadrupole parameters. A distribution of C_Q and η_Q is most likely present because of equal or inverted intensity ratio of the horns. Simulating the second species, responsible for the step at the high-frequency end of the spectrum, was not attempted, due to the lack of resolved spectral features.

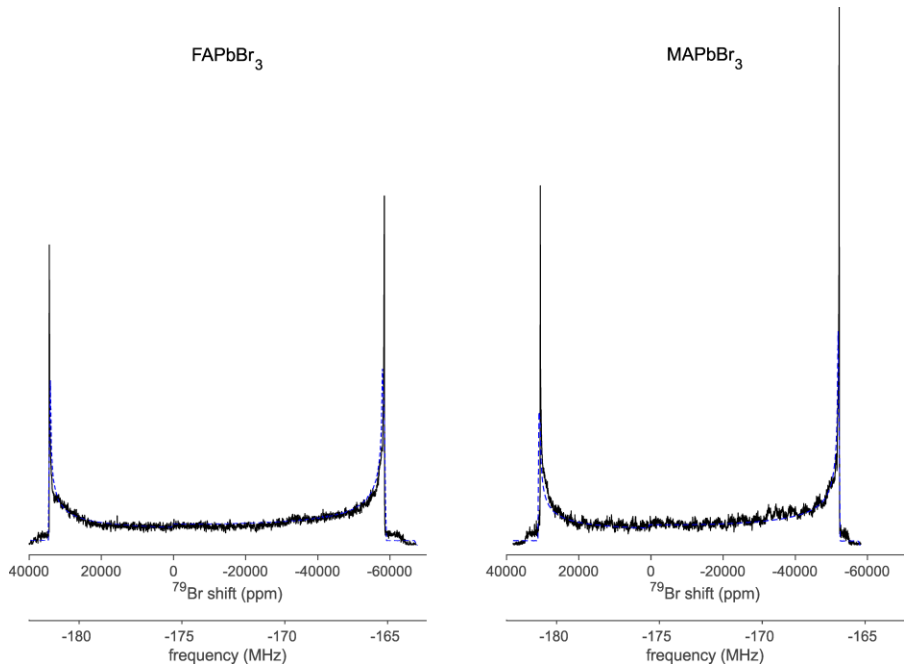

Supplementary Figure S3 | ^{79}Br static NMR spectra of bulk $FAPbBr_3$ and $MAPbBr_3$. The experimental data (solid, black lines) was simulated (dashed, blue lines) using an exact description of the quadrupole interaction, using the following parameters for $FAPbBr_3$ C_Q = 149.1034 MHz, η_Q = 0.0642, δ_{iso} = -371 ppm and for $MAPbBr_3$ C_Q = 141.0185, η_Q = 0.0099, δ_{iso} = -293 ppm.

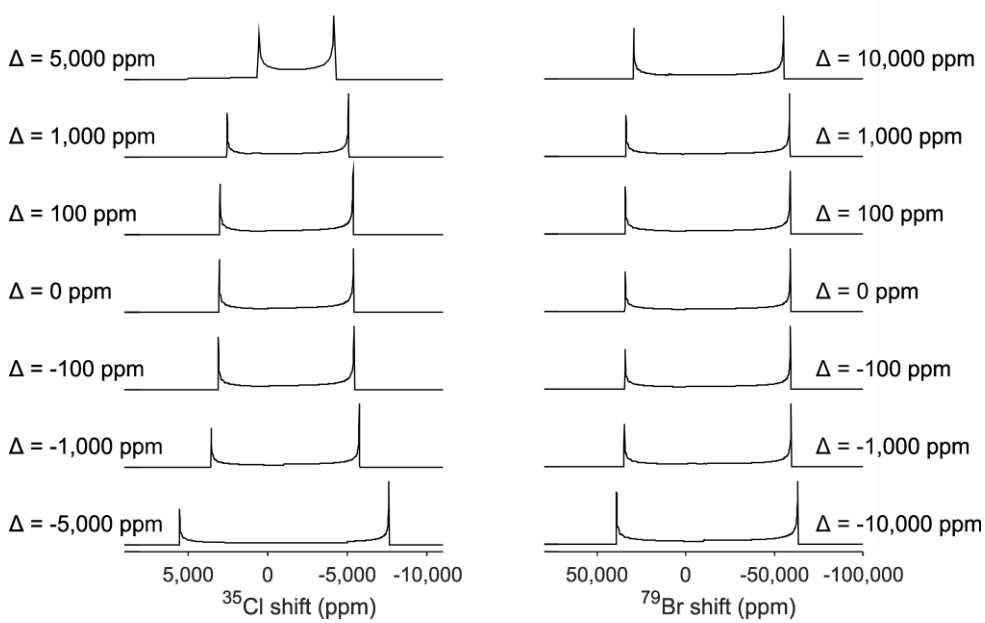

Supplementary Figure S4 | Exact simulations of ^{35}Cl and ^{79}Br NMR spectra of $CsPbCl_3$ and $CsPbBr_3$. The spectra were simulated with the QUadrupolar Exact SofTware (QUEST)[23] taking in consideration both, the quadrupole coupling and the CSA. The latter is defined by the anisotropy (Δ) and the asymmetry (η),

which are related to the principal tensor elements of the CSA: δ_{xx}, δ_{yy}, and δ_{zz}. Their values satisfy the following ordering: $|\delta_{ZZ} - \delta_{iso}| \geq |\delta_{XX} - \delta_{iso}| \geq |\delta_{YY} - \delta_{iso}|$. Thereby, the isotropic chemical shift is defined as $\delta_{iso} = (\delta_{XX} + \delta_{YY} + \delta_{ZZ})$ and the anisotropy and asymmetry are given by the following expressions: $\Delta = \delta_{ZZ} - \delta_{iso}$, and $\eta = (\delta_{YY} - \delta_{XX})/\Delta$. For the simulations, ω_0 = -58.7894 MHz and -175.4104 MHz were used as Larmor frequencies and C_Q = 15 MHz and 150 MHz as quadrupole parameters respectively. Perfect asymmetry was assumed for both nuclei and for both interactions ($\eta_Q = 0$ and $\eta_{CSA} = 0$). The PAS were set the same for both, the CSA and the EFG.

For the Larmor frequency of ^{127}I to be of equal size as the ^{127}I quadrupole couplings of lead-iodide perovskites, magnetic field strengths of approximately 35-50 T would be required. Such high magnetic fields are not likely to be easily accessible to NMR spectroscopy any time soon. Currently, even 28 T (1.2 GHz) spectrometers are not yet commercially available. The attempt to acquire a ^{127}I NMR signal of bulk $CsPbI_3$ on presently available spectrometers, such as the 16.4 T (700 MHz) at the home institution of the authors (Laboratory of Inorganic Chemistry, ETH Zurich), would be expected to produce spectra such as the one simulated in Figures 1c (γ-phase) and Supplementary Fig. S5 (δ-phase). Since neither the quadrupole nor the Zeeman terms clearly dominate the Hamiltonian in these cases, the shapes of the signals are non-trivial, and any sort of perturbation approach is inadequate. Instead, an exact description of the spin energy states is required to reconstruct the entire magnetic resonance spectrum, and this involves the diagonalization of the sum of the Zeeman and quadrupole Hamiltonians to obtain the eigenstates of the spin system. Such a simulation predicts these unfamiliar signal shapes and a very broad NMR signal (Fig. 1c and Supplementary Fig. S5). Attempting to record such NMR signals would be troublesome due to the low intensity expected from the large linewidth of more than 200 MHz. Any type of signal averaging method, such as MAS, would lead in the present case to the smearing out of the signal. Under static conditions, using the WURST-CPMG pulse sequence (see also Supplementary Note S3), as it was done in this work for $CsPbCl_3$ materials and bulk $CsPbBr_3$, recording the signal might be theoretically possible, but prohibitively long acquisition times would result due to the large number (several hundreds) of sub-spectra that would be required to sample the complete ^{127}I NMR signal. Additionally, such a spectrum would be very limited in accessible information as spectral interpretation would require simulations based on previous knowledge or on DFT calculations with long computation times. This is a general issue for lead-iodide perovskite materials due to their large quadrupole interactions. We illustrate this with the broad, atypically shaped NMR signals of γ-$CsPbI_3$ in Supplementary Fig. S5 (of C_Q = 424.3 MHz, η_Q = 0.311; C_Q = 319.7 MHz, η_Q = 0.4148) and $MAPbI_3$ in Supplementary Figure S6 (C_Q = 556.139 MHz, η_Q = 0.010; C_Q = 573.063 MHz, η_Q = 0.012).[27]

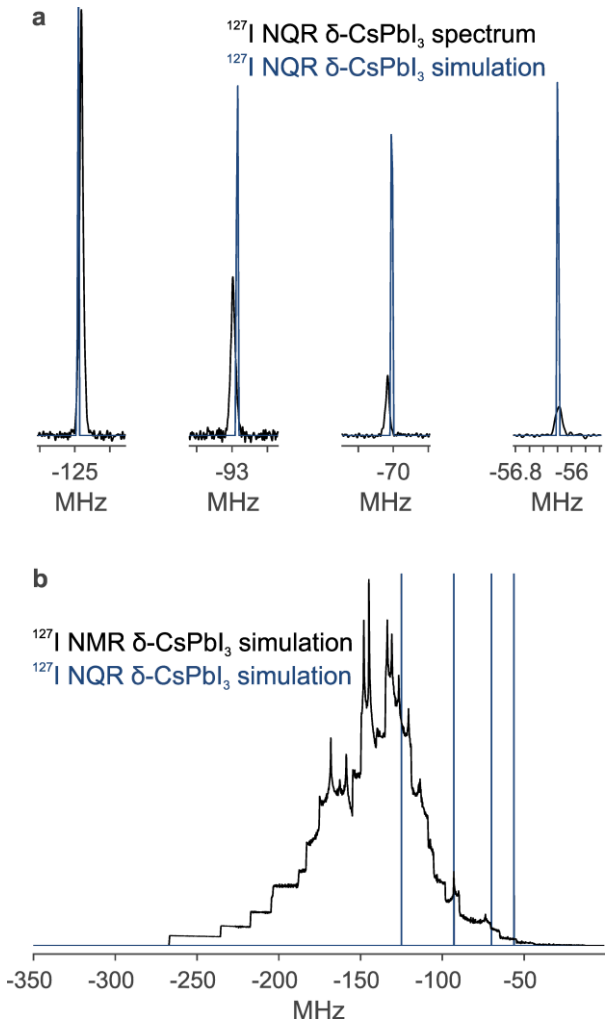

Supplementary Figure S5 | ^{127}I NQR and NMR simulation of δ-CsPbI$_3$. (a) ^{127}I NQR lines δ-CsPbI$_3$ as acquired (black) and simulated (blue). The difference in signal intensity between simulation and experimental data arises from neglecting the Boltzmann statistics in the simulation. (b) Simulated ^{127}I NMR spectrum of δ-CsPbI$_3$ powder at 16.4 T using the quadrupole parameters obtained from the ^{127}I NQR spectrum (of C_Q = 424.3 MHz, η_Q = 0.311; C_Q = 319.7 MHz, η_Q = 0.4148). The corresponding NQR resonances are plotted as superposed (dark blue) to illustrate the influence of the Zeeman splitting on the quadrupole interaction.

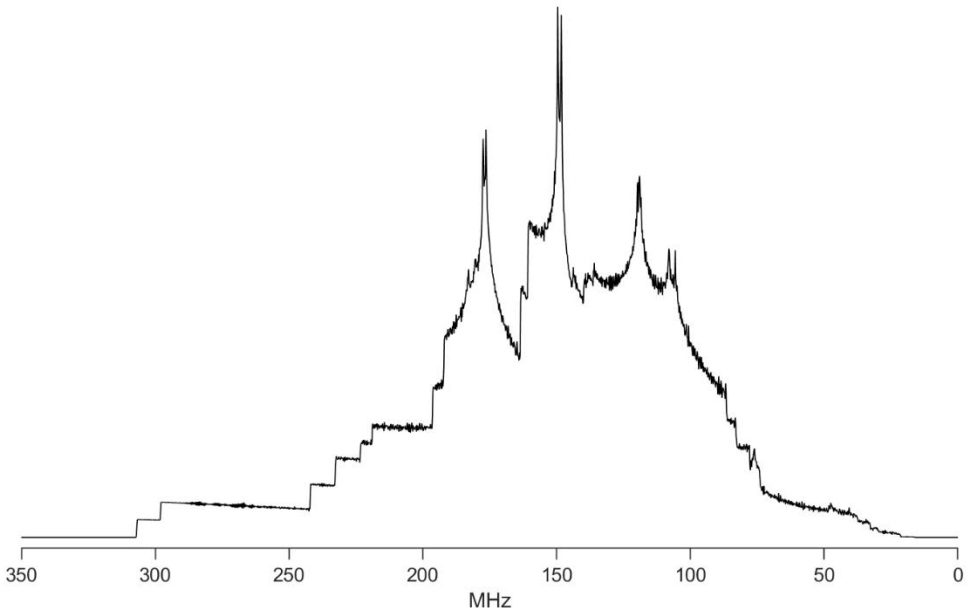

Supplementary Figure S6 | Simulated ^{127}I NMR spectrum of $MAPbI_3$. This is an exact simulation of the ^{127}I NMR spectrum of $MAPbI_3$ at 16.4 T. The following quadrupole parameters were used, as reported in literature:[31] C_Q = 528.1 MHz, η_Q = 0.29; C_Q = 558.6 MHz, η_Q = 0.34.

Supplementary Note S3. Quadrupolar nuclei and the acquisition of their NMR spectra

Most of the elements in the periodic table feature isotopes with spins $I > {}^1/_2$, which thus possess a non-vanishing quadrupole moment. The latter couples with the gradient of the electric field generated by charges present in the system, *i.e.* other nuclei and electrons. This is called the quadrupole interaction. Its strength can vary by several orders of magnitude depending on the size of the EFG and quadrupole moment described by a second rank tensor. The quadrupole moment is, like the gyromagnetic ratio, a nucleus-specific, constant property, different for every isotope. The quadrupole interaction is generally among the larger spin interactions present in NMR, usually exceeding the chemical shielding or the dipole-dipole interaction. Occasionally, the quadrupole interaction can dominate over the Zeeman interaction, in which case NMR is not the appropriate spectroscopic method to study such a spin system but NQR is preferred as discussed further below.

The effect of quadrupole couplings on NMR spectra depends on the nature of the sample. In solution-state NMR, the quadrupole interaction usually manifests itself only through accelerated spin relaxation of the quadrupole spin and of neighboring nuclei. No line-shape changes other than signal broadening is observed, due to the fast, isotropic tumbling of nuclei in solution. In solution-state NMR, the quadrupole interaction is averaged over time, similarly as it is the case for other anisotropic interactions such as the CSA.[36] For large quadrupole interactions, the signal of the quadrupolar nucleus is oftentimes too broad to be resolvable from noise as it relaxes too quickly to be detected. The anisotropy of the quadrupole interaction translates into an orientation dependence of the quadrupole interaction. As a consequence in solid-state NMR, the random alignment of the crystallites in powdered samples leads to very broad powder patterns since every crystallite orientation aligns differently relative to the external, applied magnetic field and produces a different resonance frequency. This produces so-called powder averaged spectra with inhomogenously broadened linewidths, and their line shapes encode the symmetry of the EFG. The span of frequencies that are induced by large quadrupole interactions can reach hundreds of MHz and the line shapes can vary dramatically depending on the spin multiplicity of the quadrupolar nucleus, the symmetry of the EFG and its size relative to the Zeeman interaction. Although the acquisition and interpretation of quadrupole spectra is much more challenging than for spectra of nuclear spins $I = ½$, the large size of the interaction makes it very sensitive to small changes in the EFG which directly reflect the chemical and electronic structure of the spin surrounding.

The quadrupole Hamiltonian describes the quadrupole interaction:

$$\hat{H}_Q = \frac{eQ}{2I(2I-1)\hbar}\,\hat{\vec{I}}\cdot\boldsymbol{V}\cdot\hat{\vec{I}} \qquad (1)$$

Thereby, eQ is the quadrupole moment, constituted of the elementary charge e and the tabulated, isotope-specific constant Q. I is the spin quantum number, $\hbar$ is the reduced Planck constant, $\hat{\vec{I}}$ is

the spin vector operator and $\boldsymbol{V}$ is the matrix describing the EFG, whose elements are defined as follows:

$$V_{\alpha\beta} = \frac{\partial^2 U}{\partial\alpha\partial\beta} \qquad \alpha, \beta = x, y, z \qquad (2)$$

U stands for the electrostatic potential generated by surrounding charges (electrons and other atomic nuclei) in the center of the studied nucleus. $V_{\alpha\beta}$ are the Cartesian components of the second rank, symmetrical, but purely anisotropic tensor $\boldsymbol{V}$. In the principal axis system (PAS) X, Y, Z of the EFG, $\boldsymbol{V}$ is diagonal:

$$\boldsymbol{V} = \begin{pmatrix} V_{XX} & 0 & 0 \\ 0 & V_{YY} & 0 \\ 0 & 0 & V_{ZZ} \end{pmatrix} \qquad (3)$$

Herein, capital letters are used for the PAS, while lower case letters are used for a general axis system. Since the charge distribution generating the electrostatic potential is external to the nucleus, the Laplace equation $V_{XX} + V_{YY} + V_{ZZ} = 0$ holds for $\boldsymbol{V}$ and using the convention $|V_{XX}| \leq |V_{YY}| \leq |V_{ZZ}|$, the EFG can be fully parametrized with solely the asymmetry parameter

$$\eta_Q = \frac{V_{XX} - V_{YY}}{V_{ZZ}} \qquad (4)$$

and the quadrupole constant

$$C_Q = \frac{eQV_{ZZ}}{h} \qquad (5)$$

The asymmetry parameter describes the deviation of the EFG from axial symmetry and the quadrupole constant characterizes the strength of the quadrupole interaction. While η_Q can only take values between 0 and 1, C_Q can exhibit values from a few Hz up to hundreds of MHz. In a fully isotropic surrounding, for example in perfect tetrahedral, octahedral or cubic sites, $C_Q = 0$ as the quadrupole interaction is averaged by symmetry.

A robust approach to record very wide NMR spectra, such as the ones from halide spins, involves acquiring stepwise sub-spectra with varying frequency offsets under static conditions. For more efficient excitation, adiabatic pulses, such as WURST[37] are used within an echo-train such as the CPMG sequence,[38-39] as described in several reviews.[40-42] This approach has been applied in this work to record static bulk $CsPbCl_3$ (Fig. 3 and Supplementary Fig. S2), bulk $CsPbBr_3$ (Fig. 5 and Supplementary Fig. S3) and $CsPbCl_3$ NC (Fig. 3 and Supplementary Fig. S2) NMR spectra. It is to our knowledge the first time that the WURST-CPMG sequence is applied to lead-halide perovskite materials.

Supplementary Note S4. Comparison of signal-to-noise in ^{35}Cl NMR spectra

The NMR signal scales linearly with both the sample quantity and the number of scans. At the same time, the noise increases as a square-root of the number of scans (ns) and hence the signal-to-noise (S/N) also scales as $\sqrt{ns}$. Hence NMR signals of different forms of the same $CsPbX_3$ material (bulk, nanocrystals (NCs), *etc*.) may be properly compared only when taking S/N and normalizing it to the number of scans and sample quantity (when all other experimental parameters are maintained the same).

The experimental S/N values were obtained with the measurement routine from the Topspin® program provided by Bruker to control the NMR spectrometers. Supplementary table S3 also presents typical quantities of $CsPbCl_3$ in the experiment, being systematically smaller for NCs due to the contribution of the organic capping ligand (16 weight% from thermogravimetric analysis). Furthermore, much larger number of scans was applied in the experiments with NCs.

The comparison of S/N values, normalized by both the weight and the number of scans, shows that the signal of NCs is 2-6 times weaker than bulk at 100 K and 25-32 times weaker at 273 K. As discussed in the Main text, it is the difference in the spin relaxation that leads to the much smaller amount of signal obtained from the same number of nuclei in the case of NCs.

Supplementary Table S3. Summary of signal parameters to compare S/Ns between bulk and nanocrystalline $CsPbCl_3$ ^{35}Cl NMR spectra

	Bulk $CsPbCl_3$	$CsPbCl_3$ NCs
Sample mass	~35-45 mg	~17-32 mg
Inorg. mass	~35-45 mg	~14-27 mg
ns @ 100 K	64	384
ns @ 273 K	1024	327’680
S/N @ 100 K	~70	~23
S/N @ 273 K	~107	~42
S/N normalized to 1 ns @ 100 K	~9	~1
S/N normalized to 1 ns @ 273 K	~3	~0.1
S/N normalized to 1 ns & to 1 g sample material @ 100 K	~192-246	~44-84
S/N normalized to 1 ns & to 1 g sample material @ 273 K	~74-94	~3-5

Supplementary Note S5. Relaxation and chemical exchange in halide magnetic resonance spectra of $CsPbX_3$ perovskites

Introduction to T_1 and T_2 relaxation

T_1 relaxation (longitudinal relaxation or spin-lattice relaxation) and T_2 relaxation (transverse relaxation or spin-spin relaxation) are phenomenological descriptions of the magnetization behavior and are often not exclusively based on stochastic relaxation processes. T_1 describes how fast the relaxation returns to its equilibrium state after excitation, and T_2 describes how fast the signal dephases. T_1 is always larger than T_2 due to energy conservation. Spin-spin relaxation is produced, for example, by nuclear dynamics and magnetic field fluctuations. Theoretically, T_2 corresponds to the decay rate of the free induction decay (FID). In practice, other contributions or so-called inhomogeneous contributions, produce signal dephasing and eventually an accelerated signal decay.

Usually, the dominant mechanism for spin relaxation is the fluctuation of the dipole coupling strengths with neighboring spins, which are subject to small atomic motion. Another important factor influencing relaxation times of quadrupolar nuclei are the temporal fluctuations of the local EFG. In solution-state NMR, Brownian motion is usually the major driving force for relaxation. In solid-state NMR, the relaxation times correlate directly to internal motion within the sample, *e.g.* rotations or vibrations. Hence, signal decay rates are interesting probes to determine dynamics in solids, which is sensitive to slower motions. However, interpretation of relaxation time constants from solid-state NMR experiments is challenging as incoherent contributions are difficult to distinguish from effects due to molecular dynamics.

In NMR and in NQR alike, the signal linewidth and T_1 and T_2 relaxation times are influenced by nuclear motion and therefore comprise information about structural dynamics inside the sample. Overall, NQR provides the same information as NMR regarding the quadrupolar interaction as well as the derived structural and dynamical insights.

Introduction to chemical exchange

Chemical exchange is a phenomenon involving the displacement of nuclei in a system in equilibrium. The structure of the system after chemical exchange is indistinguishable from the structure prior to exchange. Only the surrounding of the individual spin is changing, which can lead to a variety of effects in the NMR spectrum depending on which timescale it occurs. Chemical exchange is a very vast field within NMR spectroscopy, which we cannot extensively discuss here. The interested reader is referred to the comprehensive collection of reviews discussing chemical exchange.[43-58]

Chemical exchange can affect the NMR and NQR spectra in diverse ways: line shape deformation, simple line-broadening, influencing relaxation times, or giving rise to additional signals. In which way chemical exchange affects the spectrum depends on the rate of the nuclei exchange relative to the timescale of the NMR experiment. Three major chemical exchange regimes can be defined. When the exchange rate is much smaller than the difference between the resonance frequencies of the involved nuclear spins, one speaks about slow exchange. If the rate is much larger than the difference between resonance frequencies, it is called fast exchange; when the exchange rate is of the same order as the difference between resonance frequency, the system is in the intermediate regime.

In the slow exchange regime, the linewidth is influenced by the exchange rate. Detecting the chemical exchange can be challenging as there are numerous contributions to the linewidth; but with the proper experimental design, the precise determination of exchange rates is possible. For instance, in selective inversion T_1 experiments.[59]. Since the nuclei exchange on the time scale of the experiment (*i.e.* a nucleus might, but does not have to, have exchanged between the beginning and the end of the experiment), 2D exchange spectroscopy (EXSY)[60] can be performed. By varying the exchange time (also called mixing time), approximate exchange rates can be deduced. An estimate of the exchange rate can also be obtained from the ratio of the cross-peak to diagonal peak volume.

In the intermediate exchange regime coalescence is observed, and the spectral features, *i.e.* resonance frequency and linewidths, change drastically upon small changes in the experimental conditions, such as temperature or concentration. The evaluation of this parameter dependence permits the determination of exchange rates. However, simulations could be required for complex spin systems.

In the fast exchange regime, the signals have a Lorentzian line shape and the linewidth is seldom defined by the chemical exchange anymore. Nuclei can exchange multiple times during an NMR experiment. In this regime, chemical exchange is best observed by the dependence of the rate of signal dephasing during an echo train experiment. When the echo delay is shorter than the time a nucleus requires to exchange, the FID dephases slowly. However, as soon as the echo delay is longer than the exchange rate, signal dephasing occurs rapidly as the magnetization cannot be refocused due to the changed surrounding of the individual spin. In relaxation dispersion experiments,[61-67] which are often applied to study protein dynamics,[68] a series of echo trains are acquired with varying echo delay times. The exchange rate is then approximated to the delay time when the signal dephasing accelerates.

Discussion of ^{35}Cl NMR relaxation times

T_1 times usually increase with decreasing temperature as atomic and molecular motion are reduced and the corresponding fluctuations of the local magnetic field decrease. This is also the behavior we found for T_1 times in bulk and nanocrystalline $CsPbCl_3$ NCs (Fig. 3b). It is noteworthy, that the

NC's spin-lattice relaxation times are systematically shorter than the ones of bulk, which could be explained by a higher concentration of defects, *e.g.* surface termination and surface induced rearrangement, or by larger mean square thermal displacement, which probably all induce faster and/or more frequent local magnetic field fluctuations. T_1 times were obtained by fitting the evolution of the integral of the whole signal with increasing recovery delays. A qualitatively better fit could be obtained with a stretched exponential function, but this leads to larger uncertainty in the fit parameters. Hence, a mono-exponential fit function was chosen, keeping in mind that the obtained T_1 time is most likely the dominant value from a distribution of relaxation environments of the ^{35}Cl spin within the sample.[69]

T_2 times describe how fast the signal (*i.e.* the FID) decays. The T_2 times of bulk $CsPbCl_3$ dramatically increase by around two orders of magnitude when cooling from around 273 K to 200 K. This behavior is expected, since atomic and molecular dynamics, which contribute to the signal dephasing, slow down or freeze at lower temperature. Opposite to this, T_2 times of $CsPbCl_3$ NCs are independent of temperature within the experimental error and remain constant at *ca.* 1-2 ms over a temperature range of 100-300 K. The more rapid loss of coherence in the FID of ^{35}Cl nuclei contributes to the lower signal-to-noise in the spectra of $CsPbCl_3$ NCs. This reduces the number of acquirable echoes in the CPMG train and results in lower signal intensity. This faster loss of coherence in the $CsPbCl_3$ NC FIDs compared to that of bulk $CsPbCl_3$ is apparent when comparing the CPMG echo-train decay rates of both samples, which we call T_2 times for simplicity (Fig. 3c). The CPMG echo-trains of bulk and nanocrystalline $CsPbCl_3$ are well described by a mono-exponential function that includes a scaling and an offset parameter to match the experimental data. The T_2 times are obtained from the negative inverse exponent.

At 100 K, the signal of bulk $CsPbCl_3$ decays about 100-times slower than in NCs. This means that, in the CPMG echo-train, about half of the initial echo intensity is still detected after 325 ms and almost 1200 echoes later. In comparison, at the same temperature, the FID of $CsPbCl_3$ NCs has completely decayed after only 8 ms and 30 refocusing echoes. By increasing the temperature, the T_2 times of bulk $CsPbCl_3$ remain rather unaffected until 200 K, at which point they dramatically decrease until attaining values of around 8 ms at 273 K, and almost reaching decay rates found in $CsPbCl_3$ NCs. T_2 times above 273 K could not be determined, possibly due to the ferroelastic phase transitions and softening of phonon modes in bulk $CsPbCl_3$ when approaching RT, thus impeding NMR signal detection.[70-77] In NCs, these appear to be absent, or occur at higher temperatures since ^{35}Cl NMR spectra could be acquired without difficulties at RT.

The dramatic dissimilarities in value and in the temperature dependence between the $CsPbCl_3$ nanocrystalline and bulk ^{35}Cl NMR T_2 times, which are not reflected in the T_1 times, is surprising. The most plausible explanation for this observation is, in our opinion, dynamic processes such as chemical exchange in the fast regime (*i.e.* the exchange rate is shorter than the frequency difference of the exchanging spins). Most relaxation-rate-influencing interactions, such as dipole-dipole coupling, CSA, *etc.* induce spin-state fluctuations, which influence both T_1 and T_2. Chemical

exchange is a dynamic equilibrium between structurally indistinguishable states of spin systems. In other words, chemical exchange is a phenomenon of structural dynamics (as opposed to spin dynamics) that is present in a system in equilibrium.[43] Exchange rates faster than the acquisition time can accelerate the dephasing of the signal as refocusing fails for spins which have exchanged. As a result, the apparent T_2 times will be shorter. The chemical exchange hypothesis is further supported by the acceleration of signal dephasing with longer echo delay times. When echo delays of the CPMG trains are increased, the FID of the ^{35}Cl NMR signal of bulk and nanocrystalline $CsPbCl_3$ decays faster. Series of FIDs during WURST-CPMG echo-trains are plotted in Supplementary Figure S7 and S8, which are similar to the relaxation dispersion experiments[61-67] that are often used to study protein dynamics.[68] An abrupt decrease of the T_2 times is observed in both bulk and nanocrystalline $CsPbCl_3$ when increasing the echo-delay time from 0.5 to 1.3 ms, which defines the range for the exchange rate. Since the drop-in decay rate occurred at the same echo delay times in NCs and in bulk, the sampled dynamic process is the same. More processes must be present and determine the overall T_2 times of NCs and bulk; however, they are out of reach for these relaxation dispersion-type experiments. It is remarkable that the ^{35}Cl NMR T_2 times of $CsPbCl_3$ NCs (1-2 ms) are similar to the time range obtained from the echo-trains. This indicates that there must be more chemical exchange processes occurring at an equal or faster rate. Faster atomic or molecular dynamics in NCs compared to bulk appear reasonable. NCs possess a larger mean square thermal displacement and a higher density of defects than bulk, mostly due to the large specific surface area, as well as the reduced lattice constraints due to the small size of the crystallites. All these are factors that help the crystal structure to accommodate widespread atomic motion. Accelerated dynamical processes and chemical exchange in $CsPbCl_3$ NCs would be consistent with the fast anion exchange reaction reported for lead halide perovskite NCs.[78-79] Actually, chemical exchange has been already detected in ^{207}Pb NMR spectra of bulk $FAPbCl_{1.5}Br_{1.5}$ and $MAPbCl_xBr_{3-x}$ (x = 0-3) by the Michaelis group using 2D EXSY experiments.[80-81] They conclude that the exchange of Cl and Br ions occurs on the range of µs-ms. However, the measurements of the influence of chemical exchange on relaxation time performed in the present work does not necessarily involve bond breaking and dislocation of atoms as it is the case for the mixed halide perovskites studied by the Michaelis group.[80-81] Alternative dynamics, which could lead to the observation of chemical exchange in NMR or NQR are concerted distortions of the lattice through torsion, stretching or compression of the $PbCl_6$ octahedra and other phonon modes. All these forms of structure dynamics do not involve any bond breaking nor do they change the overall average structure of the lead-halide perovskite, yet they influence spin surrounding. In this study, ab-initio molecular dynamics is used to assess whether low-energy structure dynamics is enhanced in the NCs as compared to the bulk material (see the Main Text and Supplementary Figures S10 and S11.)

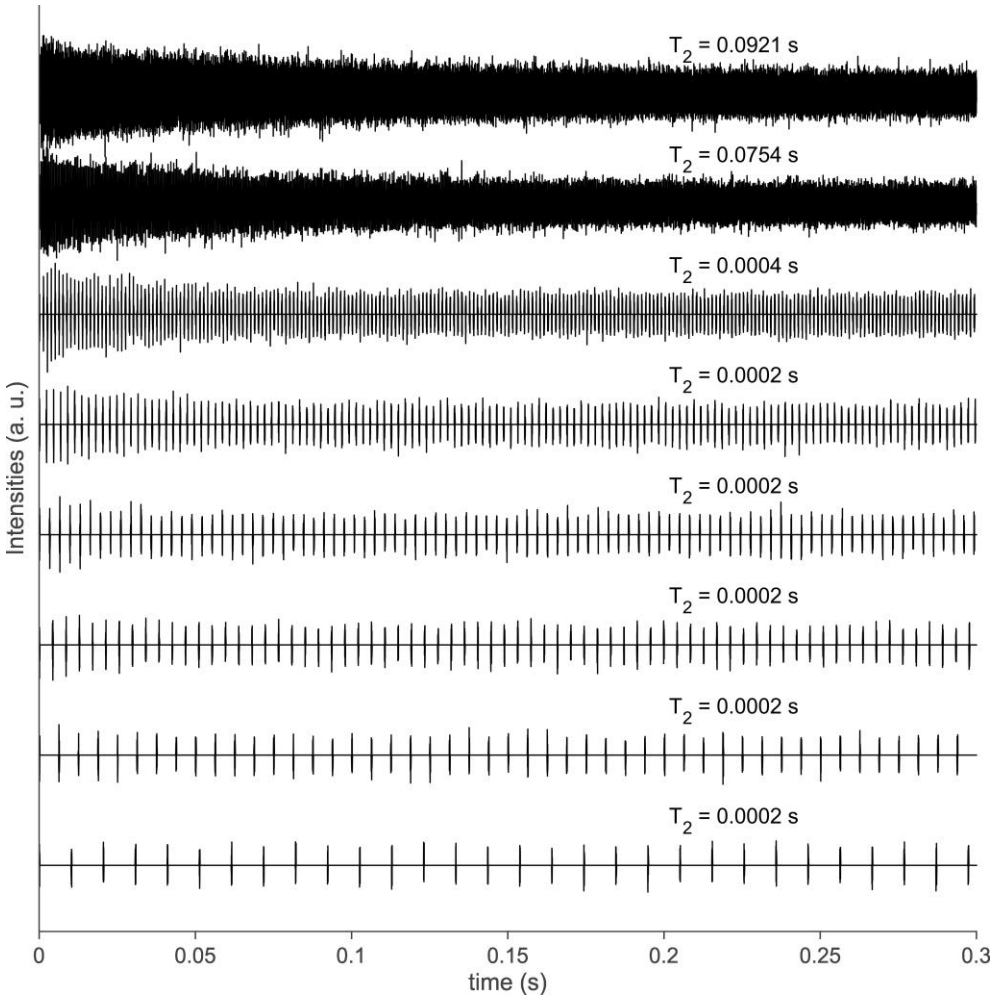

Supplementary Figure S7 | ^{35}Cl NMR FIDs of bulk $CsPbCl_3$ acquired with a WURST-CPMG pulse sequence at 250 K. From top to bottom, the echo delays were increased from 272 µs, 452 µs, 1.252 ms, 2.252 ms, 3.252 ms, 4.252 ms, 6.252 ms, to 10.252 ms. For all the experiments, T_2-times were determined; however, confidence intervals were large due to poor signal-to-noise ratio. This series of experiments resembles relaxation dispersion studies in proteins.[61-67]

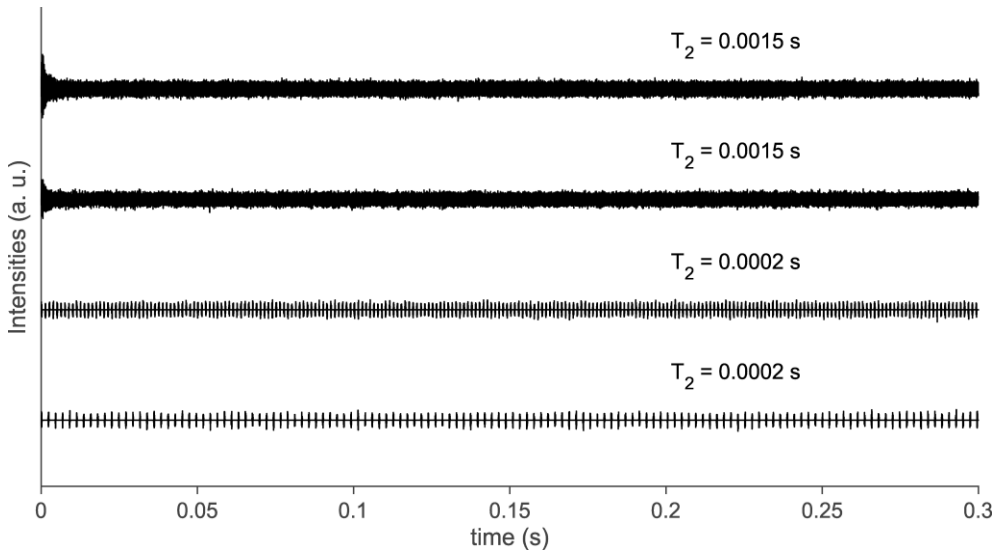

Supplementary Figure S8 | ^{35}Cl NMR FIDs of $CsPbCl_3$ NCs acquired with a WURST-CPMG pulse sequence at 250 K. From top to bottom, the echo delays were increased from 272 µs, 452 µs, 1.252 ms, 2.252 ms to 3.252 ms. For all the experiments, T_2-times were determined, however confidence intervals were large due to poor signal-to-noise ratio. This series of experiments is reminiscent of relaxation dispersion studies.[61-67]

Discussion of ^{79}Br NQR relaxation times

We have shown that the analysis and comparison of ^{35}Cl NMR relaxation times of bulk and nanocrystalline material provide a better understanding for dynamics present in these materials. A similar approach was applied also to their bromide cousins. Analogously to bulk $CsPbCl_3$, chemical exchange is also readily detectable in bulk $CsPbBr_3$, and likely exists in the corresponding NC materials as well, although it could not be experimentally evidenced due to the very low NC signal intensities. T_2 times of the bulk ^{79}Br NQR signal exhibit a dependency on the echo-delay times used in the CPMG echo-train experiments. For echo delays of 20 µs, T_2 times between 1.49 ms and 2.42 ms are obtained, while T_2 time values decrease to 0.13-0.18 ms for echo delays of 110 µs. These results set the range for the rate constants of present dynamics to about 0.1-2.4 ms in bulk $CsPbBr_3$, commensurate to that found for bulk $CsPbCl_3$ (0.5-1.3 ms).

Generally, it is puzzling that ^{79}Br NMR and NQR signals of bulk $CsPbBr_3$ are comparably easy to detect while cumbersome experimental conditions at low temperatures and highly sensitive equipment are required to acquire signals from $CsPbBr_3$ NCs. One possible explanation can be obtained by comparing the ^{79}Br NQR relaxation times of bulk $CsPbBr_3$ (Fig. 5c and 5d) with the ^{35}Cl NMR relaxation times of bulk and nanocrystalline $CsPbCl_3$ (Fig. 4b and 4c). The ^{79}Br NQR T_1 times increase with decreasing temperature, similarly to the ^{35}Cl NMR T_1 times of $CsPbCl_3$ (Fig. 5c). Within experimental error, the ^{79}Br T_1-times of the two NQR lines cannot be distinguished. Also, the T_2 times of the two ^{79}Br NQR transitions of $CsPbBr_3$ are comparable; they are about 1-2 orders of magnitude faster than T_1 times, depending on the echo delay time used (short echo delays

of 20 µs, light markers; long echo delays of 110 µs, dark markers in Fig. 5d). Overall, the ^{35}Cl NMR relaxation times of bulk $CsPbCl_3$ are 1-2 orders of magnitude slower than the ^{79}Br NQR relaxation times of bulk $CsPbBr_3$. If also in $CsPbBr_3$ NCs the relaxation is 1-2 orders of magnitude faster than in $CsPbCl_3$ NCs, an extremely fast signal dephasing, on the order of 50-500 µs, would be extrapolated for $CsPbBr_3$ NCs (from 0.7-1.9 ms values of $CsPbCl_3$ NCs). These are time scales which are barely or not detectable by NMR and NQR spectroscopy, independently of the utilized electronics. By the time the excitation pulse has rung down, the signal from the ^{79}Br spins in $CsPbBr_3$ will be significantly reduced or will have completely decayed. This explains the low signal intensity found at 90 K, as it represents the small fraction of the signal which has not decayed by the time when FID acquisition starts. Furthermore, such fast T_2-times rationalize our incapacity to detect ^{79}Br NMR signals of $CsPbBr_3$ NCs at RT as the signal would presumably decay even faster than at 90 K and be completely dephased before the acquisition has begun. The results of the comparison of the ^{79}Br NQR and ^{35}Cl NMR relaxation times must be interpreted with caution since the interactions dominating relaxation and signal dephasing phenomena may differ in contribution and in nature in NMR and NQR.

Supplementary Figure S9.

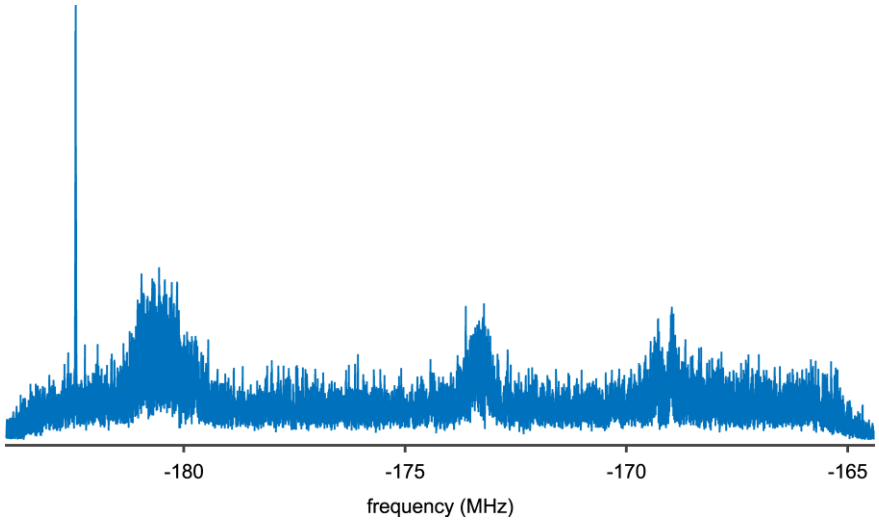

Supplementary Figure S9 | Background NMR signal from the probe. Background signal obtained over the ^{79}Br NMR frequency range at 16.1 T of lead-bromide perovskite signals when the rotor is filled with a bromine-free sample (glycine). The sharp signal at -182.4 MHz is attributed to the metallic aluminium shield of the probe. The other background signals could not be identified but are suspected to (at least partially) originate from plastic (carbon-containing) components of the probe. The very long T_2 of most of the background allowed to reduce its impact on the sample signal by discarding later echoes of the CPMG-train.

Supplementary Figure S10.

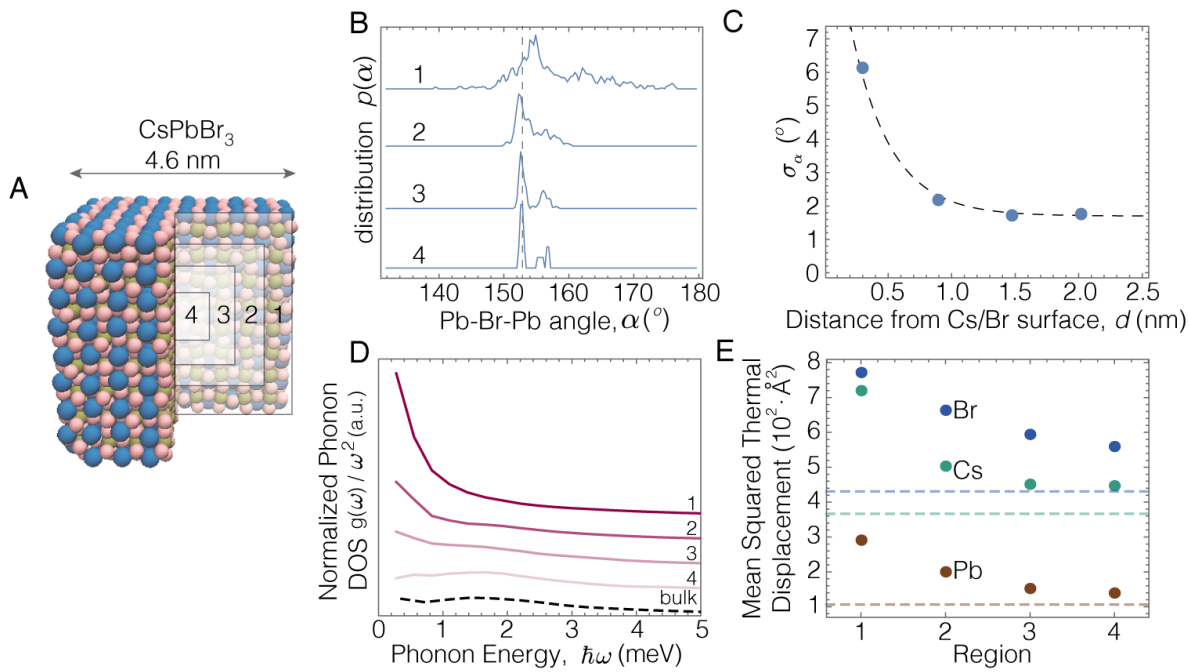

Supplementary Figure S10 | *Ab-Initio* calculations of $CsPbBr_3$ NCs. (A) Atomistic model of a 4.6 nm $CsPbBr_3$ NC, with a cross-section removed to indicate the four regions of interest within the NC. (B) Plots of the statistical distribution of Pb-Br-Pb angles, α, within each region of the NC. (C) Standard deviation of α as a function of distance of the Br atom from the surface of the NC, d. (D) Plot of the partial phonon density of states in each of the four regions of the NC, normalized to the phonon frequency squared. The dashed line is that calculated for bulk $CsPbBr_3$. (E) Plot of the mean-squared-thermal-displacement, $\langle u^2 \rangle$, of each atom type in each of the 4 regions of the NC. The dashed lines correspond to the $\langle u^2 \rangle$ calculated for bulk $CsPbBr_3$.

Supplementary Figure S11.

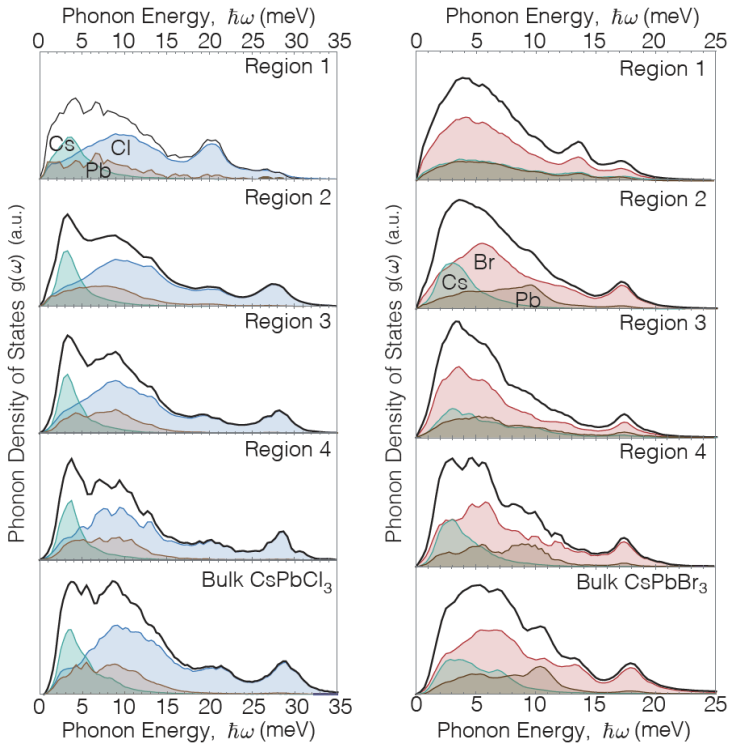

Supplementary Figure S11 | Phonon Density of States. The computed partial phonon density of states, and partial density of states for each atom type, of the $CsPbCl_3$ (left panel) and $CsPbBr_3$ (right panel) NCs, in each of the four regions of the NC (see Figure 4 and Figure S10). The phonon density of states of bulk orthorhombic $CsPbCl_3$ and $CsPbBr_3$ are given in the bottom row of each panel.

Supplementary Note S6. Density functional theory calculations of the EFGs and quadrupole parameters of the halide spins in $CsPbBr_3$

The calculations of EFG tensors of halide spins in $CsPbBr_3$ were performed using Vienna ab-initio simulation package (VASP) code. The projector augmented wave (PAW)[82-83] potentials for atoms were used. For generalized gradient approximation (GGA) Perdew-Burke-Ernzerhof exchange-correlation functional (PBE)[84-85] was used. A single cell comprising 20 atoms with a kinetic energy cut-off of 237 eV and an automatic γ-centered mesh of 11x11x11 k-points were used. Ionic minimization was performed until all forces on atoms wee smaller than 0.001 eV/Å. A mixture of blocked Davidson iteration scheme and subsequent residual minimization scheme, direct inversion in the iterative subspace (RMM-DIIS) algorithm was used for the electronic optimization. Spin-orbit coupling (SOC) was not taken into account due to known self-interaction error that raises valence band maximum.[86-87] This result is fortuitous, because the position of conduction and valence band edges is wrong but their difference, which makes the band gap, is close to experimental value. As a result, the combination of PBE and SOC produces a very poor match with experiment. On the other hand, hybrid functionals in combination with SOC were reported to reproduce experimental values much more accurately.[88] Hybrid calculations considering the SOC are computationally more expensive. For the relative comparison of EFG values for the step-wise structural change, GGA without SOC calculation has proven to be sufficiently accurate. EFG tensors were calculated using the PAW method as implemented in the VASP code.[89]

The quadrupole parameters calculated for various structures of $CsPbBr_3$ are plotted in Supplementary Figure S12. The studied structures of $CsPbBr_3$ encompass the highly symmetric cubic perovskite structure over to orthorhombic distorted structures obtained by gradual tilting of the $PbBr_6$ octahedra.

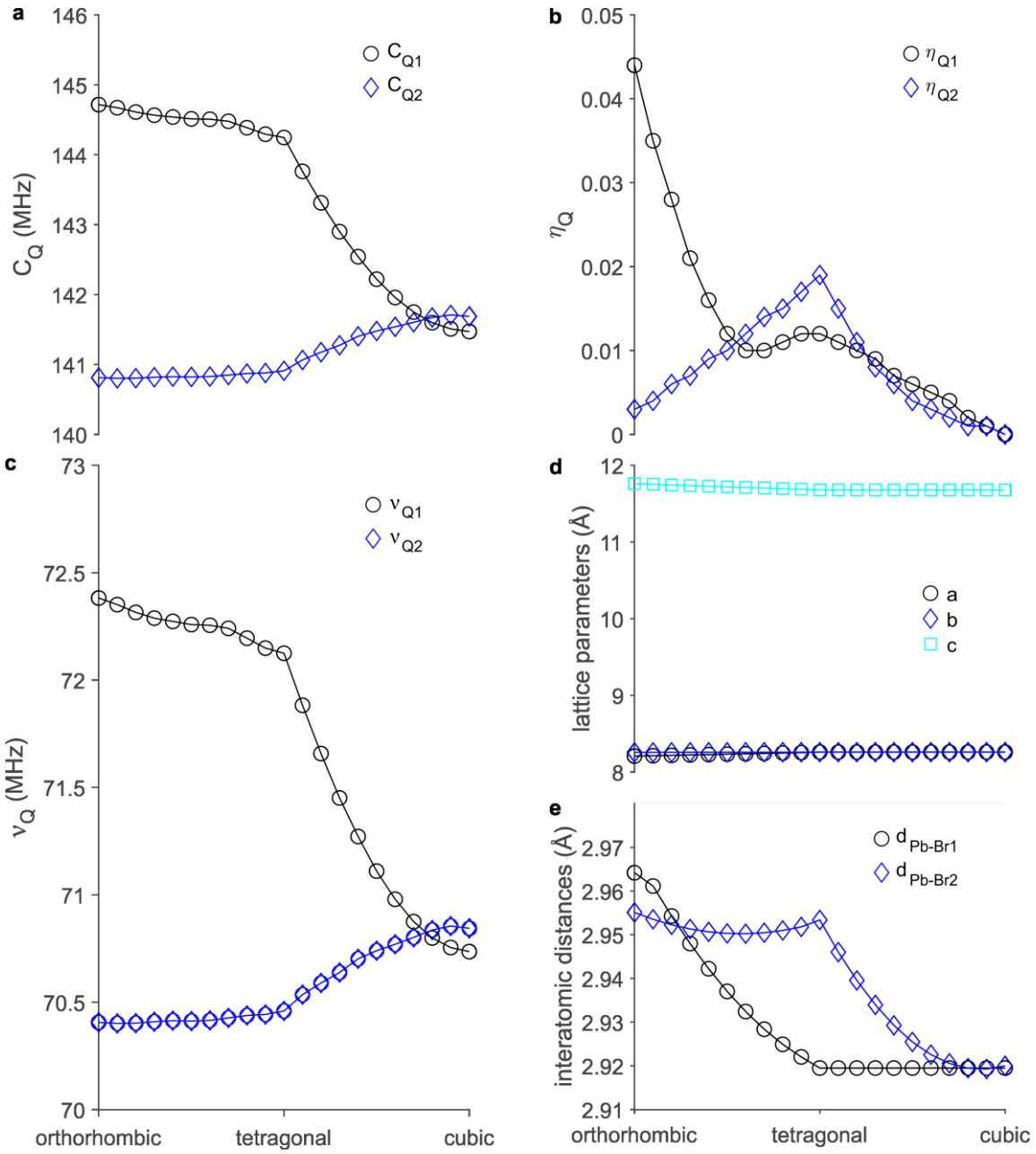

Supplementary Figure S12 | ^{79}Br quadrupole and crystal structure parameters of $CsPbBr_3$ by DFT calculations. DFT calculations of the ^{79}Br quadrupole parameters [C_Q in (a) and η_Q in (b)] and the NQR resonance frequencies (c) of the bromine species in various $CsPbBr_3$ perovskite structures. The latter are obtained by gradual tilting of the octahedra, thereby gradually reducing the symmetry from cubic over tetragonal to orthorhombic crystal structure. The symmetry breaking in non-cubic structures leads to inequality of the bromine atoms, hence the occurrence of two bromine species. Although the calculated quadrupole parameters deviate from experimental data by about 10%, tendencies such as high sensitivity of the C_Q towards the structure of $CsPbBr_3$ is retained, as can be seen from the small changes in crystal lattices (d) and lead-bromide distances (e) in the different structures. The spectral resolution of NMR and NQR spectrometers are in the order of sub-Hz, much below the deviations of quadrupole parameters, which occur in the kHz-MHz range.

Supplementary Table S4. Spectra parameters of ^{127}I NQR signals from different $CsPbI_3$ materials

Experimental ^{127}I NQR frequencies, FWHM and T_2 relaxations of bulk γ-$CsPbI_3$, bulk δ-$CsPbI_3$ and $CsPbI_3$ NCs. The quadrupole interaction constants ($C_Q = e^2Qqh^{-1}$) and the asymmetry parameter (η_Q) were calculated according to literature.[90] The background had a T_2 relaxation time of ≤0.02 ms.

Sample	ν / MHz	FWHM / kHz	T_2 / ms	C_Q / MHz	η_Q
γ-$CsPbI_3$ bulk	-77.75	159.4	0.14	517.98	0.025
	-155.34	295.8	0.13		
	-81.50	171.4	0.17	537.36	0.101
	-160.88	279.3	0.15		
δ-$CsPbI_3$ bulk	-56.21	102.8		319.82	0.414
	-92.98	81.6			
	-70.10	60.6		424.21	0.313
	-124.90	70.4			
$CsPbI_3$ NCs	-77.79	95.1	0.07	518.12	0.029
	-155.41	157.1	0.06		
	-81.42	287.8	≤ 0.02	537.01	0.100
	-160.78	165.8	≤ 0.02		

Supplementary Figure S13.

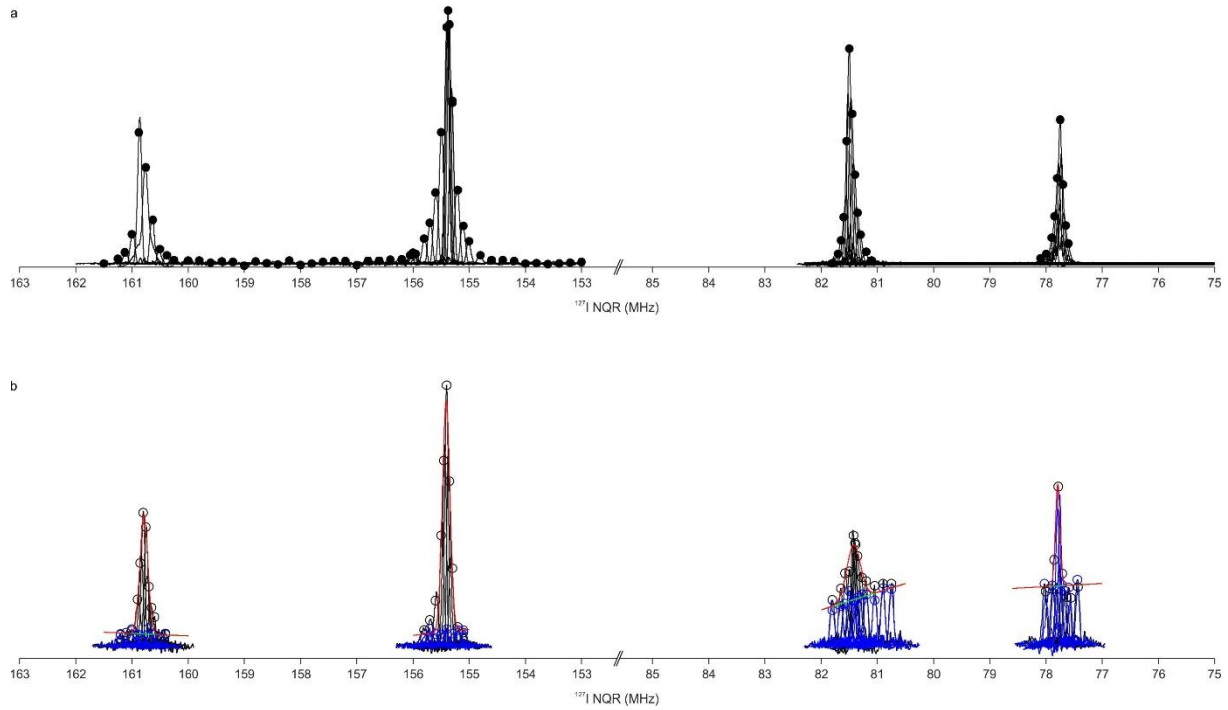

Supplementary Figure S13 | ^{127}I NQR spectra of bulk γ-$CsPbI_3$ and $CsPbI_3$ NCs. In the case of the bulk (a), the spectrum was reconstructed from several sub-spectra (individual thin lines) at different carrier frequencies, by taking only the intensity at the carrier frequency (black points). For the NCs (b), first, the background (in blue) had to be subtracted. The background was determined by measuring with a rotor filled with glycine and fitting the intensities at the carrier frequencies. This was then used as a baseline for the fitting of the NC signals. Such procedure was not required for the bulk signal due to its much larger intensity leading to the background signal not exceeding noise level.

Supplementary Methods

Ab-initio calculations

Ab-initio calculations were performed within the CP2K program suite using the quickstep module.[91] Calculations were carried out using a dual basis of localized Gaussians and plane-waves,[92] with a 300Ry plane-wave cut-off. Double-Zeta-Valence-Polarization (DZVP),[93] Goedecker–Teter–Hutter pseudopotentials[94] for core electrons, and the PBE exchange correlation functional were used. In all calculations, convergence to 10^{-8} in Self-Consistent Field is enforced. For the calculations on NCs, non-periodic boundary conditions in atomic coordinates and electric potential were used, through the use of a wavelet Poisson solver.[95] Geometry optimization was performed with the Quickstep module using the Broyden–Fletcher–Goldfarb–Shannon (BFGS) optimizer. All atoms in were systems are relaxed using maximum force of 24 meVÅ^{-1} as convergence criteria. For bulk calculations, Cell optimizations of the orthorhombic unit cell was performed, with convergence to 100 bar. AIMD simulations were performed in the NVT ensemble at 300K, with a 10 fs step size, using a CSVR (canonical sampling through velocity rescaling) thermostat.[96] To equilibrate the temperature and total energy, 2 ps were run with a thermostat time constant of 15 fs, after which the time constant is switched to 1 ps, and the AIMD is run for a minimum of 13 ps. The first 3 ps of the AIMD are discarded for data analysis, and trivial translation and rotation of the entire NC is removed from the atomic trajectories.[96] We note that while we include the charge compensation from the ligands in the calculations, we did not explicitly include the ligands themselves. Full charge compensation from ligands for the NC here would require 17 ligands, and given that there are 378 surface Cs atoms available for bonding, we do not expect significant deviation of the structure with the inclusion of ligands.

The four regions of the NCs (Figure 4a in the main text and Figure S10a in SI) are defined by cutting up the NC into concentric regions, where each region contains one Cs-halide and Pb-halide layer. For the Pb-halide-Pb bonding angles, the distance from the NC surface is determined from the midpoint between the Pb atoms. Note that for binning of the Pb-halide-Pb angles in the four regions, angles between Pb atoms in two different layers are grouped into the outer layer. The specific binning for the $CsPbCl_3$ NC presented in the main text is shown in Figure S14. The regions were identically defined for the $CsPbBr_3$ NC presented in the SI.

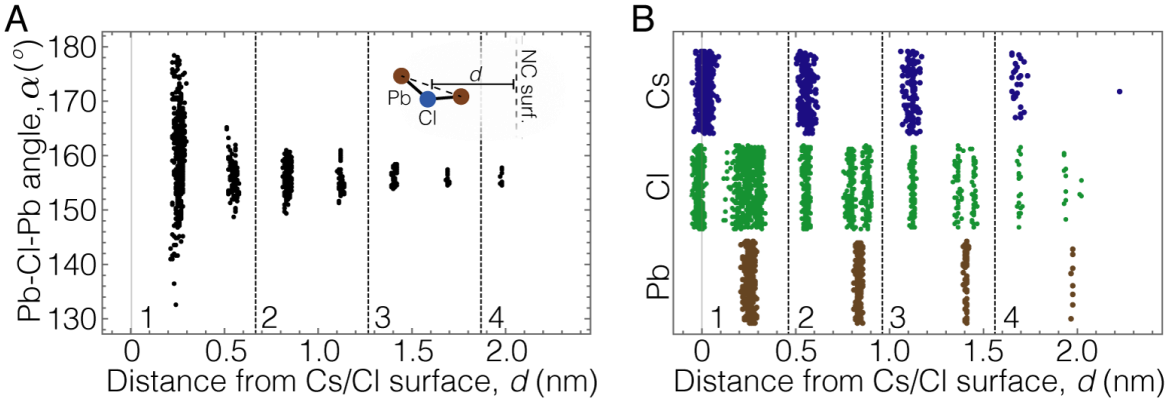

Figure S14 | Binning of Pb-Cl-Pb angles and atom positions for the $CsPbCl_3$ NC presented in the main text. A) plot of the Pb-Cl-Pb bonding angles as a function of distance from the NC surface, with dashed lines indicating binning regions used for computing the distribution of angles used in Fig. 4b and 4c of the main text. B) Plot of the distance for each atom in the NC from the NC surface. Points are randomly scattered on the vertical axis for clarity. The dashed lines represent the regions used for binning the mean-squared displacement and partial-phonon density of states in Fig. 4d and 4e of the main text.

Materials

Bulk $CsPbX_3$

Bulk *$CsPbCl_3$* and δ-*$CsPbI_3$* powders crystallized from concentrated aqueous HX (X = Cl, I) containing PbX_2 and CsX with adaptations from earlier literature.[97-98] PbX_2 (5 mmol) were dissolved in 7.5 mL of concentrated aqueous HX (37% HCl or 57% HI) and then mixed with aqueous CsX (5 mmol in 1 mL of water), yielding the respective $CsPbX_3$ powders. The latter were washed three times with ethanol and dried under vacuum.

Bulk $CsPbBr_3$ powders were obtained from finely crushed $CsPbBr_3$ single crystals. The latter were synthesized using the inverse temperature crystallization method as described in literature,[99] from CsBr and $PbBr_2$ solutions in dimethylsulfoxide, mixed with cyclohexanol and dimethylformamide.

Bulk γ-$CsPbI_3$ was synthesized by heating δ-$CsPbI_3$ to 600 K and quenching by rapidly cooling to RT, following the procedure from Sutton *et al.*[11] The black powder still contained δ-$CsPbI_3$ impurities according to powder X-ray diffraction (XRD).

$CsPbX_3$ NCs

$CsPbCl_3$ and *$CsPbBr_3$ NCs* were synthesized using the hot-injection method of Krieg *et al.*,[100] using zwitterionic capping ligands and with metal oleates as precursors. Lead(II)-oleate, cesium-oleate and the C_3-sulfobetaine (ligand) were mixed in octadecene and heated to 150 °C (for chloride) or 130 °C (for bromide). At these temperatures, $TOPX_2$ (X = Cl, Br; a halide source) was injected via syringe and the reaction mixture was quickly cooled to RT. Purification and size-selection was performed by repeated dissolution/precipitation with toluene and ethylacetate, respectively, as a solvent and antisolvent.

$CsPbI_3$ NCs were prepared by reacting PbI_2 with cesium-oleate using, in the presence of oleic acid and oleylamine as capping ligands, as described by Protesescu *et al.*[101] Cesium-oleate was injected to a hot PbI_2-ligand solution in octadecene (170 °C) and quickly cooled to RT. Purification and size-selection was performed by repeated dissolution/precipitation with hexane and methylacetate.

The quality of NCs was confirmed by the optical absorption and photoluminescence spectroscopies, powder XRD (not shown) and transmission electron microscopy (TEM, Supplementary Fig. S15)

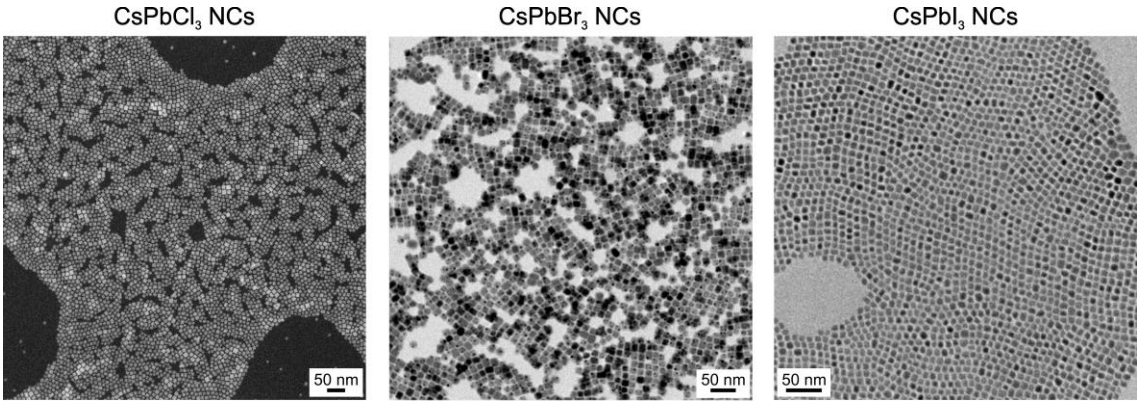

Figure S15 | HAADF-STEM image of $CsPbCl_3$ NCs and TEM images of $CsPbX_3$ NCs (X = Cl, Br, I). These NCs exhibit mean edge length of 8.5 nm, 13 nm and 8 nm, respectively. The STEM image was recorded with a high-angle annular dark field (HAADF) detector on an aberration-corrected HD2700CS microscope (Hitachi) at an acceleration voltage V_{acc} = 200 kV. The TEM images were recorded on a Hitachi HT7700 microscope operating at 100 kV or on a JEOL JEM-1400 Plus microscope operated at 120 kV.

Experimental details about NMR and NQR experiments

Figure 3a: ^{35}Cl NMR spectra of $CsPbCl_3$ NCs and bulk $CsPbCl_3$

Powders of $CsPbCl_3$ NCs and bulk $CsPbCl_3$ were ground with a mortar when necessary and packed into 3.2 mm sapphire rotors.

A WURST-CPMG pulse sequence as described by O'Dell and Schurko[102] was used to acquire sub-spectra at different frequency offsets. The individual echoes of the sub-spectra were apodised with a $\cos^2$-function and summed before Fourier transformation (FT). From the superposition of all processed sub-spectra in magnitude mode, the skyline was taken to yield the complete signal of a $CsPbCl_3$ material at a certain temperature. The sample was left in the probe head when changing the temperature from one experiment to another to avoid metastable phases.

Acquisition parameters for ^{35}Cl NMR WURST-CPMG sub-spectra of $CsPbCl_3$ NCs	
Magnetic field	14.1 T
Larmor frequency (MHz)	58.7894
Temperature (K)	100, 150, 200, 250, 273
Rotor diameter (mm)	3.2
Pulse Sequence	WURST-CPMG
Number of scans	384, 2048, 24576, 65536, 327680
frequency offset (ppm/kHz)	0/0, -2501/-147.0, -5003/-294.1
Recycle delay (s)	5.0, 1.0, 0.5, 0.1, 0.05
Spectral width (kHz)	1500
Spinning frequency (Hz)	0
Acquisition length (number of points)	24972
echo delay (µs)	111
number of echoes	30
WURST pulse type	WURST-80[37]
WURST pulse length (µs)	50
Numb. of points in WURST pulse	1000
Excitation width	1 MHz
Sweeping direction	Low to high frequency

Acquisition parameters for ^{35}Cl NMR WURST-CPMG sub-spectra of bulk $CsPbCl_3$	
Magnetic field	14.1 T
Larmor frequency (MHz)	58.7894
Temperature (K)	100, 150, 200, 250, 273
Rotor diameter (mm)	3.2
Pulse Sequence	WURST-CPMG
Number of scans	64, 64, 128, 512,1024
frequency offset (ppm/kHz)	0/0, -2501/-147.0, -5003/-294.1
Recycle delay (s)	10.0, 5.0, 2.0, 0.5,0.5

Spectral width (kHz)	1500
Spinning frequency (Hz)	0
Acquisition length (number of points)	24972
echo delay (µs)	111
number of echoes	30
WURST pulse type	WURST-80[37]
WURST pulse length (µs)	50
Numb. of points in WURST pulse	1000
Excitation width	1 MHz
Sweeping direction	Low to high frequency

Figure 3b and 3c: ^{35}Cl NMR T_1- and T_2-times of $CsPbCl_3$ NCs and bulk $CsPbCl_3$

Powders of $CsPbCl_3$ NCs and bulk $CsPbCl_3$ were ground with a mortar when necessary and packed into 3.2 mm sapphire rotors.

^{35}Cl NMR T_1 time constants were obtained by fitting the integral of processed WURST-CPMG acquired with different recovery delays using the following mono-exponential function:

$$Integral(\tau) = c_1\left(1 - e^{-\tau/T_1}\right) + c_2$$

Next to T_1, a scaling factor c_1 and an offset c_2 were optimized in order to fit experimental data. Integral(τ) is the integral of the processed spectrum at the recovery delay time τ. Spectra were processed in a similar way as for Figure 3a, except for using only one sub-spectrum per temperature for reasons of experimental time expenses. As pulse sequence for the spectra acquired at different recovery delay times τ a WURST-CPMG sequence as described by O'Dell and Schurko[102] was used. The individual echoes of the spectra were apodised with a $\cos^2$-function and summed before FT. Integration was done on the magnitude mode spectra. The experiments were performed on the same samples as in Figure 3a and were conducted right before the acquisition of the spectrum in Figure 3a of the corresponding temperature.

Acquisition parameters for ^{35}Cl NMR T_1 Experiments on $CsPbCl_3$ NCs	
Magnetic field	14.1 T
Larmor frequency (MHz)	58.7894
Temperature (K)	100, 150, 200, 250, 273, 295
Rotor diameter (mm)	3.2
Pulse Sequence	WURST-CPMG
Number of scans	256 – 5696
frequency offset (ppm/kHz)	-2501/-147.0
Recycle delay (s)	0.1 – 5.0
Spectral width (kHz)	1500

Spinning frequency (Hz)	0
Acquisition length (number of points)	24972
echo delay (µs)	111
number of echoes	30
WURST pulse type	WURST-80[37]
WURST pulse length (µs)	50
Numb. of points in WURST pulse	1000
Excitation width	1 MHz
Sweeping direction	Low to high frequency

Acquisition parameters for ^{35}Cl NMR T_1 experiments on bulk $CsPbCl_3$	
Magnetic field	14.1 T
Larmor frequency (MHz)	58.7894
Temperature (K)	100, 150, 200, 250, 273
Rotor diameter (mm)	3.2
Pulse Sequence	WURST-CPMG
Number of scans	64 – 521
frequency offset (ppm/kHz)	-2501/-147.0
Recycle delay (s)	0.1 – 5.0
Spectral width (kHz)	1500
Spinning frequency (Hz)	0
Acquisition length (number of points)	24972
echo delay (µs)	111
number of echoes	30
WURST pulse type	WURST-80[37]
WURST pulse length (µs)	50
Numb. of points in WURST pulse	1000
Excitation width	1 MHz
Sweeping direction	Low to high frequency

^{35}Cl NMR T_2-time constants were obtained by fitting the integral of the higher horn in the spectra of the individual echoes of the CPMG echo-train. Only the most intense parts were used for better signal-to-noise and hence more precise fit results as only a qualitative interpretation is aspired for. Fits of the right horn yielded comparable T_2-time constants. The following monoexponential function was used for the fit:

$$Integral(\tau) = c_1 e^{-\tau/T_2} + c_2$$

Next to T_2, a scaling factor c_1 and an offset c_2 were optimized in order to fit experimental data. Integral(τ) is the integral of the echo appearing at time τ in the FID. Similar as to the T_1-time measurements, only one sub-spectrum was used for every temperature for reasons of experimental time expenses. As pulse sequence for the spectra acquired at every temperature, a WURST-CPMG sequence as described by

O'Dell and Schurko[102] was used. The FID was segmented into the individual echoes generated by the CPMG sequence. Each echo was then Fourier transformed, set to magnitude mode and integrated separately.

Acquisition parameters for ^{35}Cl NMR T_2 experiments on $CsPbCl_3$ NCs	
Magnetic field	14.1 T
Larmor frequency (MHz)	58.7894
Temperature (K)	100, 150, 200, 250, 273, 295
Rotor diameter (mm)	3.2
Pulse Sequence	WURST-CPMG
Number of scans	384 – 327680
frequency offset (ppm/kHz)	-2501/-147.0
Recycle delay (s)	0.05 – 5.0
Spectral width (kHz)	1500
Spinning frequency (Hz)	0
Acquisition length (number of points)	24972
echo delay (µs)	111
number of echoes	30
WURST pulse type	WURST-80[37]
WURST pulse length (µs)	50
Numb. of points in WURST pulse	1000
Excitation width	1 MHz
Sweeping direction	Low to high frequency

Acquisition parameters for ^{35}Cl NMR T_2 experiments on bulk $CsPbCl_3$	
Magnetic field	14.1 T
Larmor frequency (MHz)	58.7894
Temperature (K)	100, 150, 200, 250, 273
Rotor diameter (mm)	3.2
Pulse Sequence	WURST-CPMG
Number of scans	242 – 8192
frequency offset (ppm/kHz)	0/0,
Recycle delay (s)	0.5 – 10.0
Spectral width (kHz)	1500
Spinning frequency (Hz)	0
Acquisition length (number of points)	979692
echo delay (µs)	111
number of echoes	1200
WURST pulse type	WURST-80[37]
WURST pulse length (µs)	50
Numb. of points in WURST pulse	1000
Excitation width	1 MHz
Sweeping direction	Low to high frequency

Figure 5a: ^{79}Br NMR of bulk $CsPbBr_3$

Bulk $CsPbBr_3$ single crystals were ground with a mortar to be packed into a 4 mm zirconia rotor for the NMR experiment and into a 3.2 mm sapphire rotor for the NQR experiment.

For the acquisition of the ^{79}Br NMR signal of bulk $CsPbBr_3$, a WURST-CPMG pulse sequence as described by O'Dell and Schurko[102] was used to acquire 41 sub-spectra at different frequency offsets, under static conditions and at RT. The difference in frequency between offsets was chosen to be a multiple of the inverse of the echo delay in order for the spikelet of the FT sub-spectra to overlap. Sub-spectra were truncated after 1212 points and the 3 remaining echoes were apodized individually with a $\cos^2$-function. After reconstruction and zero-filling up to the initial acquisition length the FID the sub-spectra were FT and superposed to take the skyline spectrum.

Acquisition parameters for ^{79}Br NMR WURST-CPMG sub-spectra of bulk $CsPbBr_3$	
Magnetic field	16.4 T
Larmor frequency (MHz)	175.4104
Temperature	RT
Rotor diameter (mm)	4
Pulse Sequence	WURST-CPMG
Number of scans	8192
frequency offset (ppm/kHz)	45607.3/8000 - -52448.4/-9200
Recycle delay (s)	0.1
Spectral width (kHz)	2000
Spinning frequency (Hz)	0
Acquisition length (number of points)	53248
echo delay (µs)	75
number of echoes	64
WURST pulse type	WURST-80[37]
WURST pulse length (µs)	50
Numb. of points in WURST pulse	1000
Excitation width	1 MHz
Sweeping direction	Low to high frequency

Figure 5b: NQR spectra of bulk and nanocrystalline $CsPbBr_3$

Powders of bulk and nanocrystalline $CsPbBr_3$ were ground with a mortar to be filled into a Teflon® tube of 2 mm diameter, which was closed on both sides with home-made Teflon®-plugs.

Due to the narrow detection width of the probe several sub-spectra had to be acquired to sample the complete signal width. The sub-spectra were acquired with a conventional Hahn echo pulse sequence. Pulse ringing and excess noise were truncated for every echo, and the FIDs were Fourier transformed and phased. Phasing of the spectra was facilitated by the collection of full echoes. From the superposition of all sub-spectra the complete spectrum was generated by taking the skyline.

Acquisition parameters for ^{79}Br NQR spectra of bulk $CsPbBr_3$	
Magnetic field	0 T
Temperature	90 K, 200 K 298 K
Sample diameter (mm)	2
Pulse Sequence	Hahn echo
Number of scans	1024
Carrier frequency (MHz)	66.80 - 67.35
Recycle delay (ms)	50
Spectral width (kHz)	20’000
Spinning frequency (Hz)	0
Acquisition length (number of points)	8192
echo delay (µs)	10
90° pulse length (µs)	6.5

Acquisition parameters for ^{79}Br NQR spectra of $CsPbBr_3$ NCs	
Magnetic field	0 T
Temperature	90 K
Sample diameter (mm)	2
Pulse Sequence	Hahn echo
Number of scans	10’000
Carrier frequency (MHz)	66.53 - 67.555
Recycle delay (ms)	40
Spectral width (kHz)	20’000
Spinning frequency (Hz)	0
Acquisition length (number of points)	8192
echo delay (µs)	10
90° pulse length (µs)	6.5

Figure 5c and d: T_1- and T_2-times of bulk $CsPbBr_3$

Bulk $CsPbBr_3$ single crystals were ground with a mortar to be packed into a 3.2 mm sapphire rotor for T_2-time measurements. For the T_1-time measurements the same powder was filled into a Teflon® tube of 2 mm diameter, which was closed on both sides with home-made Teflon®-plugs.

^{79}Br NQR T_1 time constants were obtained by fitting the integral of processed Hahn echoes acquired after a saturating pulse train with different recovery delays using the following mono-exponential function:

$$Integral(\tau) = c_1\left(1 - e^{-\tau/T_1}\right) + c_2$$

Next to T_1, a scaling factor c_1 and an offset c_2 were optimized in order to fit experimental data. Integral(τ) is the integral of the processed spectrum at the recovery delay time τ. Before integration of the signal, pulse ringing and excess noise were truncated, and the FIDs were Fourier transformed and phased. Phasing of the spectra was facilitated by the collection of full echoes.

Acquisition parameters for ^{79}Br NQR T_1 Experiments on bulk $CsPbBr_3$	
Magnetic field	0 T
Temperature (K)	90, 120, 200, 250, 273, 295
Sample diameter (mm)	2
Pulse Sequence	Satrec-Hahn echo
Number of scans	128 – 256
Carrier frequency (MHz)	66.80 – 70.36
Recycle delay (ms)	0.005 – 2’621.4
Spectral width (kHz)	25’000
Spinning frequency (Hz)	0
Acquisition length (number of points)	4096
echo delay (µs)	50
90° pulse length (µs)	6
180° pulse length for inversion pulse (µs)	12

^{79}Br NQR T_2 time constants were obtained by fitting the integral of the individual echoes from the QCPMG echo-train using the following mono-exponential function:

$$Integral(\tau) = c_1 e^{-\tau/T_2} + c_2$$

Next to T_2, a scaling factor c_1 and an offset c_2 were optimized in order to fit experimental data. Integral(τ) is the integral of the echo appearing at time τ in the FID. A conventional QCPMG pulse sequence was used as provided by Bruker. The FIDs were segmented into the individual echoes generated by the QCPMG echo-train. Each echo was then Fourier transformed, set to magnitude mode and integrated separately.

Acquisition parameters for ^{79}Br NQR T_2 Experiments on bulk $CsPbBr_3$	
Magnetic field	0 T
Temperature (K)	100, 150, 200, 250, 295
Rotor diameter (mm)	3.2
Pulse Sequence	QCPMG
Number of scans	4096
Carrier frequency (MHz)	66.8000 - 70.1322
Recycle delay (s)	0.05
Spectral width (kHz)	1250
Spinning frequency (Hz)	0
Acquisition length (number of points)	2048
echo delay (µs)	20, 110
90° pulse length (µs)	2.75

Figure 6: ^{127}I NQR spectrum of $CsPbI_3$ NCs and bulk $CsPbI_3$

All $CsPbI_3$ samples were handled in a glovebox. Bulk $CsPbI_3$ powder was packed as synthesized into a 4 mm sapphire rotor. NCs were dried under vacuum and packed as a powder into the rotor. Background spectra were acquired using a sapphire rotor filled with glycine.

For the acquisition of the ^{127}I NQR lines of bulk $CsPbI_3$ the conventional Hahn echo pulse sequence was used as provided by Bruker. Pulse ringing and excess noise were truncated and replaced by zero filling. Phasing of the spectra was facilitated by the collection of full echoes.

Acquisition parameters for ^{127}I NQR spectra on bulk $CsPbI_3$	
Magnetic field	0 T
Temperature	RT
Rotor diameter (mm)	4
Pulse Sequence	Hahn echo
Number of scans	16384
Carrier frequency (MHz)	77.4 - 81.8, 150.0 - 161.5
Recycle delay (s)	0.001
Spectral width (kHz)	1250
Spinning frequency (Hz)	0
Acquisition length (number of points)	2048
echo delay (µs)	150
90° pulse length (µs)	4.25

Acquisition parameters for ^{127}I NQR spectra on $CsPbI_3$ NCs	
Magnetic field	0 T
Temperature	RT
Rotor diameter (mm)	4
Pulse Sequence	Hahn echo
Number of scans	16384
Carrier frequency (MHz)	77.45 - 81.8, 155.1 - 161.2
Recycle delay (s)	0.001
Spectral width (kHz)	1250
Spinning frequency (Hz)	0
Acquisition length (number of points)	2048
echo delay (µs)	138
90° pulse length (µs)	4.25

^{127}I NQR T_2 time constants were obtained by fitting the integral of the individual echoes from the QCPMG echo-train using the following mono-exponential function:

$$Integral(\tau) = c_1 e^{-\tau/T_2} + c_2$$

Next to T_2, a scaling factor c_1 and an offset c_2 were optimized in order to fit experimental data. Integral(τ) is the integral of the echo appearing at time τ in the FID. A conventional CPMG pulse sequence was used as provided by Bruker. The FIDs were segmented into the individual echoes generated by the CPMG echo-train. Each echo was then Fourier transformed, set to magnitude mode and integrated separately.

Acquisition parameters for ^{127}I NQR T_2 Experiments on bulk $CsPbI_3$ and background	
Magnetic field	0 T
Temperature (K)	295
Rotor diameter (mm)	4
Pulse Sequence	CPMG
Number of scans	87k – 2M
Carrier frequency (MHz)	77.75, 155.400, 160.875
Recycle delay (s)	0.005
Spectral width (kHz)	1000000
Spinning frequency (Hz)	0
Acquisition length (number of points)	8592
echo delay (µs)	40
90° pulse length (µs)	4.25

Acquisition parameters for ^{127}I NQR T_2 Experiments on $CsPbI_3$ NCs	
Magnetic field	0 T
Temperature (K)	295
Rotor diameter (mm)	4
Pulse Sequence	CPMG
Number of scans	4M
Carrier frequency (MHz)	77.75, 81.85, 155.375, 160.875
Recycle delay (s)	0.005
Spectral width (kHz)	1000000
Spinning frequency (Hz)	0
Acquisition length (number of points)	8592
echo delay (µs)	40
90° pulse length (µs)	4.25

References

1. Moller, C. K., Crystal structure and photoconductivity of caesium plumbohalides. *Nature* **1958,** *182* (4647), 1436-1436.

2. Poglitsch, A.; Weber, D., Dynamic disorder in methylammoniumtrihalogenoplumbates (II) observed by millimeter-wave spectroscopy. *J. Chem. Phys.* **1987,** *87* (11), 6373-6378.

3. Binek, A.; Hanusch, F. C.; Docampo, P.; Bein, T., Stabilization of the trigonal high-temperature phase of formamidinium lead iodide. *J. Phys. Chem. Lett.* **2015,** *6* (7), 1249-1253.

4. Stoumpos, C. C.; Kanatzidis, M. G., The renaissance of halide perovskites and their evolution as emerging semiconductors. *Acc. Chem. Res.* **2015,** *48* (10), 2791-2802.

5. Schueller, E. C.; Laurita, G.; Fabini, D. H.; Stoumpos, C. C.; Kanatzidis, M. G.; Seshadri, R., Crystal structure evolution and notable thermal expansion in hybrid perovskites formamidinium tin iodide and formamidinium lead bromide. *Inorg. Chem.* **2018,** *57* (2), 695-701.

6. Hirotsu, S.; Harada, J.; Iizumi, M.; Gesi, K., Structural phase transitions in $CsPbBr_3$. *J. Phys. Soc. Jpn.* **1974,** *37* (5), 1393-1398.

7. Fujii, Y.; Hoshino, S.; Yamada, Y.; Shirane, G., Neutron-scattering study on phase transitions of $CsPbCl_3$. *Phys. Rev. B* **1974,** *9* (10), 4549-4559.

8. Trots, D. M.; Myagkota, S. V., High-temperature structural evolution of caesium and rubidium triiodoplumbates. *J. Phys. Chem. Solids* **2008,** *69* (10), 2520-2526.

9. Sharma, S.; Weiden, N.; Weiss, A., Phase diagrams of quasibinary systems of the type: ABX_3 — $A'BX_3$; ABX_3 — $AB'X_3$, and ABX_3 — ABX'_3; X = halogen. *Z. Phys. Chem.* **1992,** *175* (1), 63.

10. Marronnier, A.; Roma, G.; Boyer-Richard, S.; Pedesseau, L.; Jancu, J.-M.; Bonnassieux, Y.; Katan, C.; Stoumpos, C. C.; Kanatzidis, M. G.; Even, J., Anharmonicity and disorder in the black phases of cesium lead iodide used for stable inorganic perovskite solar cells. *ACS Nano* **2018,** *12* (4), 3477-3486.

11. Sutton, R. J.; Filip, M. R.; Haghighirad, A. A.; Sakai, N.; Wenger, B.; Giustino, F.; Snaith, H. J., Cubic or orthorhombic? Revealing the crystal structure of metastable black-phase $CsPbI_3$ by theory and experiment. *ACS Energy Lett.* **2018,** *3* (8), 1787-1794.

12. Chi, L.; Swainson, I.; Cranswick, L.; Her, J.-H.; Stephens, P.; Knop, O., The ordered phase of methylammonium lead chloride $CH_3ND3PbCl_3$. *J. Solid State Chem.* **2005,** *178* (5), 1376-1385.

13. Chen, C.; Hu, X.; Lu, W.; Chang, S.; Shi, L.; Li, L.; Zhong, H.; Han, J.-B., Elucidating the phase transitions and temperature-dependent photoluminescence of $MAPbBr_3$ single crystal. *J. Phys. D: Appl. Phys.* **2018,** *51* (4), 045105.

14. Whitfield, P. S.; Herron, N.; Guise, W. E.; Page, K.; Cheng, Y. Q.; Milas, I.; Crawford, M. K., Structures, phase transitions and tricritical behavior of the hybrid perovskite methyl ammonium lead iodide. *Sci. Rep.* **2016,** *6*, 35685.

15. Protesescu, L.; Yakunin, S.; Bodnarchuk, M. I.; Bertolotti, F.; Masciocchi, N.; Guagliardi, A.; Kovalenko, M. V., Monodisperse formamidinium lead bromide nanocrystals with bright and stable green photoluminescence. *J. Am. Chem. Soc.* **2016,** *138* (43), 14202-14205.

16. Weber, O. J.; Ghosh, D.; Gaines, S.; Henry, P. F.; Walker, A. B.; Islam, M. S.; Weller, M. T., Phase behavior and polymorphism of formamidinium lead iodide. *Chem. Mater.* **2018,** *30* (11), 3768-3778.

17. Harris, R. K.; Becker, E. D.; Cabral de Menezes, S.; Goodfellow, R.; Granger, P. NMR nomenclature. Nuclear spin properties and conventions for chemical shifts. *Pure Appl. Chem.* **2001**, *73* (11), 1795-1818.

18. Szell, P. M. J.; Bryce, D. L., Solid-state nuclear magnetic resonance and nuclear quadrupole resonance as complementary tools to study quadrupolar nuclei in solids. *Conc. Magn. Reson. A* **2016,** *45A* (6), e21412.

19. Bain, A. D., Quadrupole interactions: NMR, NQR, and in between from a single viewpoint. *Magn. Reson. Chem.* **2017,** *55* (3), 198-205.

20. Bain, A. D.; Khasawneh, M., From NQR to NMR: The complete range of quadrupole interactions. *Conc. Magn. Reson. A* **2004,** *22A* (2), 69-78.

21. Vega, A. J., Quadrupolar Nuclei in Solids. *eMagRes* **2007**.

22. Man, P. P., Quadrupolar Interactions. *eMagRes* **2007**.

23. Perras, F. A.; Widdifield, C. M.; Bryce, D. L., QUEST-QUadrupolar Exact SofTware: A fast graphical program for the exact simulation of NMR and NQR spectra for quadrupolar nuclei. *Solid State Nucl. Magn. Reson.* **2012,** *45–46*, 36-44.

24. Tovborg-Jensen, N., NQR investigation of phase transitions in cesium plumbochloride. *J. Chem. Phys.* **1969,** *50* (1), 559-560.

25. van Driel, H. M.; Armstrong, R. L., ^{35}Cl spin-lattice relaxation study of phase tansitions in $CsPbCl_3$. *Phys. Rev. B* **1975,** *12* (3), 839-841.

26. Hidaka, M.; Okamoto, Y.; Zikumaru, Y., Structural phase transition of $CsPbCl_3$ below room temperature. *Phys. Status Solidi A* **1983,** *79* (1), 263-269.

27. Xu, Q.; Eguchi, T.; Nakayama, H.; Nakamura, N.; Kishita, M., Molecular motions and phase transitions in solid $CH_3NH_3PbX_3$ (X = Cl, Br, I) as studied by NMR and NQR. In *Z. Naturforsch. A*, 1991; Vol. 46, p 240.

28. Sharma, S.; Weiden, N.; Weiss, A., Phase transitions in $CsSnCl_3$ and $CsPbBr_3$ an NMR and NQR study. *Z. Naturforsch., A* **1991,** *46* (4), 329.

29. Volkov, A. F.; Venevtsev, Y. N.; Semin, G. K., Nuclear quadrupole resonance (NQR) of ^{79}Br and ^{81}Br in perovskite and orthorhombic forms of $CsPbBr_3$ and $CsPbJ_3$. *Phys. Status Solidi B* **1969,** *35* (2), K167-K169.

30. Franssen, W. M. J.; van Es, S. G. D.; Dervişoğlu, R.; de Wijs, G. A.; Kentgens, A. P. M., Symmetry, dynamics, and defects in methylammonium lead halide perovskites. *J. Phys. Chem. Lett.* **2017,** *8* (1), 61-66.

31. Senocrate, A.; Moudrakovski, I.; Kim, G. Y.; Yang, T.-Y.; Gregori, G.; Grätzel, M.; Maier, J., The nature of ion conduction in methylammonium lead iodide: A multimethod approach. *Angew. Chem. Int. Ed.* **2017,** *56* (27), 7755-7759.

32. Senocrate, A.; Moudrakovski, I.; Maier, J., Short-range ion dynamics in methylammonium lead iodide by multinuclear solid state NMR and ^{127}I NQR. *Phys. Chem. Chem. Phys.* **2018,** *20* (30), 20043-20055.

33. Yamada, K.; Hino, S.; Hirose, S.; Yamane, Y.; Turkevych, I.; Urano, T.; Tomiyasu, H.; Yamagishi, H.; Aramaki, S., Static and dynamic structures of perovskite halides ABX_3 (B = Pb, Sn) and their

characteristic semiconducting properties by a Hückel analytical calculation. *Bull. chem. Soc. Jpn.* **2018,** *91* (8), 1196-1204.

34. Maurer, M., Electric field gradients of randomly disordered compounds. *Phys. Rev. B* **1986,** *34* (12), 8996-8999.

35. Seleznyova, K.; Sergeev, N. A.; Olszewski, M.; Stępień, P.; Yagupov, S. V.; Strugatsky, M. B.; Kliava, J., Fitting MAS NMR spectra in crystals with local disorder: Czjzek's vs. Maurer's model for ^{11}B and ^{71}Ga in polycrystalline gallium borate. *Solid State Nucl. Magn. Reson.* **2017,** *85-86*, 12-18.

36. Werbelow, L. G., Relaxation Theory for Quadrupolar Nuclei. *eMagRes* **2011**.

37. Kupce, E.; Freeman, R., Adiabatic pulses for wideband inversion and broadband decoupling. *J. MAgn. Reson. A* **1995,** *115* (2), 273-276.

38. Carr, H. Y.; Purcell, E. M., Effects of diffusion on free precession in nuclear magnetic resonance experiments. *Phys. Rev.* **1954,** *94* (3), 630-638.

39. Meiboom, S.; Gill, D., Modified spin-echo method for measuring nuclear relaxation times. *Rev. Sci. Instrum.* **1958,** *29* (8), 688-691.

40. O'Dell, L. A.; Rossini, A. J.; Schurko, R. W., Acquisition of ultra-wideline NMR spectra from quadrupolar nuclei by frequency stepped WURST–QCPMG. *Chem. Phys. Lett.* **2009,** *468* (4), 330-335.

41. Schurko, R. W., Acquisition of Wideline Solid-State NMR Spectra of Quadrupolar Nuclei. *eMagRes* **2007**.

42. Schurko, R. W., Ultra-wideline solid-state NMR spectroscopy. *Acc. Chem. Res.* **2013,** *46* (9), 1985-1995.

43. Bain, A. D., Chemical exchange in NMR. *Prog. Nucl. Magn. Reson. Spectrosc.* **2003,** *43* (3), 63-103.

44. Johnson, C. S., Chemical rate processes and magnetic resonance. In *Adv. Magn. Opt. Reson.*, Waugh, J. S., Ed. Academic Press: 1965; Vol. 1, pp 33-102.

45. Lynden-Bell, R. M., The calculation of line shapes by density matrix methods. *Prog. Nucl. Magn. Reson. Spectrosc.* **1967,** *2*, 163-204.

46. Reeves, L. W., N.M.R. measurements of reaction velocities and equilibrium constants as a function of temperature. In *Adv. Phys. Org. Chem.*, Gold, V., Ed. Academic Press: 1965; Vol. 3, pp 187-269.

47. Jesson, J. P.; Meakin, P., Determination of mechanistic information from nuclear magnetic resonance line shapes for intramolecular exchange. *Acc. Chem. Res.* **1973,** *6* (8), 269-275.

48. Binsch, G.; Kessler, H., The kinetic and mechanistic evaluation of NMR spectra. New analytical methods (18). *Angew. Chem. Int. Ed.* **1980,** *19* (6), 411-428.

49. Kessler, H., Detection of hindered rotation and inversion by NMR spectroscopy. *Angew. Chem. Int. Ed.* **1970,** *9* (3), 219-235.

50. Farrugia, L. J., Dynamics and fluxionality in metal carbonyl clusters: some old and new problems. *J. Chem. Soc., Dalton Trans.* **1997,** (11), 1783-1792.

51. Pons, M.; Millet, O., Dynamic NMR studies of supramolecular complexes. *Prog. Nucl. Magn. Reson. Spectrosc.* **2001,** *38* (4), 267-324.

52. Fielding, L., Determination of association constants (K_a) from solution NMR data. *Tetrahedron* **2000,** *56* (34), 6151-6170.

53. Orrell, K. G., Dynamic NMR Spectroscopy in Inorganic and Organometallic Chemistry. In *Annu. Rep. NMR Spectrosc.*, Webb, G. A., Ed. Academic Press: 1999; Vol. 37, pp 1-74.

54. Orrell, K. G.; Šik, V., Dynamic NMR Spectroscopy in Inorganic and Organometallic Chemistry. In *Annu. Rep. NMR Spectrosc.*, Webb, G. A., Ed. Academic Press: 1987; Vol. 19, pp 79-173.

55. Orrell, K. G.; Šik, V., Dynamic NMR Spectroscopy in Inorganic and Organometallic Chemistry. In *Annu. Rep. NMR Spectrosc.*, Webb, G. A., Ed. Academic Press: 1993; Vol. 27, pp 103-171.

56. Dong, R. Y., Relaxation and the dynamics of molecules in the liquid crystalline phases. *Prog. Nucl. Magn. Reson. Spectrosc.* **2002,** *41* (1), 115-151.

57. Johnston, E. R., Density matrix theory for calculating magnetization transfer and dynamic lineshape effects. *Conc. Magn. Reson.* **1995,** *7* (3), 219-242.

58. Brown, K. C.; Tyson, R. L.; Weil, J. A., Conformation interchange in nuclear magnetic resonance spectroscopy. *J. Chem. Educ.* **1998,** *75* (12), 1632.

59. Forsén, S.; Hoffman, R. A., Exchange rates by nuclear magnetic multiple resonance. III. Exchange reactions in systems with several nonequivalent sites. *J. Chem. Phys.* **1964,** *40* (5), 1189-1196.

60. Jeener, J.; Meier, B. H.; Bachmann, P.; Ernst, R. R., Investigation of exchange processes by two-dimensional NMR spectroscopy. *J. Chem. Phys.* **1979,** *71* (11), 4546-4553.

61. Allerhand, A.; Gutowsky, H. S., Spin-echo NMR studies of chemical exchange. I. Some general aspects. *J. Chem. Phys.* **1964,** *41* (7), 2115-2126.

62. Allerhand, A.; Gutowsky, H. S., Spin-echo NMR studies of chemical exchange. IV. Intramolecular exchange of a coupled AB system. *J. Chem. Phys.* **1965,** *42* (12), 4203-4212.

63. Allerhand, A.; Gutowsky, H. S., Spin-echo studies of chemical exchange. II. Closed formulas for two sites. *J. Chem. Phys.* **1965,** *42* (5), 1587-1599.

64. Deverell, C.; Morgan, R. E.; Strange, J. H., Studies of chemical exchange by nuclear magnetic relaxation in the rotating frame. *Mol. Phys.* **1970,** *18* (4), 553-559.

65. Carver, J. P.; Richards, R. E., A general two-site solution for the chemical exchange produced dependence of T_2 upon the Carr-Purcell pulse separation. *J. Magn. Reson.* **1972,** *6* (1), 89-105.

66. Laszlo, P., Fast kinetics studied by NMR. *Prog. Nucl. Magn. Reson. Spectrosc.* **1979,** *13* (4), 257-270.

67. Williams, M. A. K.; Halstead, T. K., An analytical form describing T_2 dispersions resulting from diffusive exchange. *Mol. Phys.* **1998,** *93* (4), 609-613.

68. Neudecker, P.; Lundström, P.; Kay, L. E., Relaxation dispersion NMR spectroscopy as a tool for detailed studies of protein folding. *Biophys. J.* **2009,** *96* (6), 2045-2054.

69. Narayanan, A.; Hartman, J. S.; Bain, A. D., Characterizing nonexponential spin-lattice relaxation in solid-state NMR by fitting to the stretched exponential. *J. Magn. Reson. A* **1995,** *112* (1), 58-65.

70. Chabin, M.; Gilletta, F., Experiment investigation of the ferroelastic domain structure in cesium lead chloride in the monoclinic phase. *J. Appl. Chrystallogr.* **1980,** *13* (6), 539-543.

71. Shin, E. J.; Jeong, H. K.; Kim, S. Y.; Jeong, J., The orientation of ferroelastic domain in single crystal, $CsPbCl_3$. *J. Korean Assoc. Cryst. Growth* **1997,** *7* (1), 117-225.

72. Lim, A. R.; Jeong, S.-Y., Ferroelastic phase transition and twin structure by ^{133}Cs NMR in a $CsPbCl_3$ single crystal. *Physica B* **2001,** *304* (1), 79-85.

73. Jeong, Hee T.; Cho, Yong C.; Cho, Chae R.; Jeong, S.-Y., Consideration on domain walls orientations in $CsPbCl_3$ ferroelastic crystal in the monoclinic phase. *J. Phys. Soc. Jpn.* **2001,** *70* (3), 717-722.

74. Hirotsu, S., Experimental studies of structural phase transitions in $CsPbCl_3$. *J. Phys. Soc. Jpn.* **1971,** *31* (2), 552-560.

75. Hirotsu, S.; Kunii, Y., Brillouin scattering study of cubic $CsPbCl_3$. *J. Phys. Soc. Jpn.* **1981,** *50* (4), 1249-1254.

76. Ohta, H.; Harada, J.; Hirotsu, S., Superstructure and phase transitions in $CsPbCl_3$. *Solid State Commun.* **1973,** *13* (12), 1969-1972.

77. Sakudo, T.; Unoki, H.; Fujii, Y.; Kobayashi, J.; Yamada, M., A new structural phase transition in $CsPbCl_3$. *Phys. Lett. A* **1969,** *28* (8), 542-543.

78. Nedelcu, G.; Protesescu, L.; Yakunin, S.; Bodnarchuk, M. I.; Grotevent, M. J.; Kovalenko, M. V., Fast anion-exchange in highly luminescent nanocrystals of cesium lead halide perovskites ($CsPbX_3$, X = Cl, Br, I). *Nano Lett.* **2015,** *15* (8), 5635-5640.

79. Akkerman, Q. A.; D'Innocenzo, V.; Accornero, S.; Scarpellini, A.; Petrozza, A.; Prato, M.; Manna, L., Tuning the optical properties of cesium lead halide perovskite nanocrystals by anion exchange reactions. *J. Am. Chem. Soc.* **2015,** *137*, 10276.

80. Askar, A. M.; Karmakar, A.; Bernard, G. M.; Ha, M.; Terskikh, V. V.; Wiltshire, B. D.; Patel, S.; Fleet, J.; Shankar, K.; Michaelis, V. K., Composition-tunable formamidinium lead mixed halide perovskites via solvent-free mechanochemical synthesis: decoding the Pb environments using solid-state NMR spectroscopy. *J. Phys. Chem. Lett.* **2018,** *9* (10), 2671-2677.

81. Karmakar, A.; Askar, A. M.; Bernard, G. M.; Terskikh, V. V.; Ha, M.; Patel, S.; Shankar, K.; Michaelis, V. K., Mechanochemical synthesis of methylammonium lead mixed–halide perovskites: unraveling the solid-solution behavior using solid-state NMR. *Chem. Mater.* **2018,** *30* (7), 2309-2321.

82. Blöchl, P. E., Projector augmented-wave method. *Phys. Rev. B* **1994,** *50* (24), 17953-17979.

83. Kresse, G.; Joubert, D., From ultrasoft pseudopotentials to the projector augmented-wave method. *Phys. Rev. B* **1999,** *59* (3), 1758-1775.

84. Perdew, J. P.; Burke, K.; Ernzerhof, M., Generalized gradient approximation made simple. *Phys. Rev. Lett.* **1996,** *77* (18), 3865-3868.

85. Perdew, J. P.; Burke, K.; Ernzerhof, M., Generalized gradient approximation made simple. *Phys. Rev. Lett.* **1997,** *78* (7), 1396-1396.

86. Du, M.-H., Density functional calculations of native defects in $CH_3NH_3PbI_3$: Effects of spin–orbit coupling and self-interaction error. *J. Phys. Chem. Lett.* **2015,** *6* (8), 1461-1466.

87. Du, M.-H., Correction to "Density functional calculations of native defects in $CH_3NH_3PbI_3$: Effects of spin–orbit coupling and self-interaction error". *J. Phys. Chem. Lett.* **2018,** *9* (14), 3799-3799.

88. Du, M. H., Efficient carrier transport in halide perovskites: theoretical perspectives. *J. Mater. Chem. A* **2014,** *2* (24), 9091-9098.

89. Petrilli, H. M.; Blöchl, P. E.; Blaha, P.; Schwarz, K., Electric-field-gradient calculations using the projector augmented wave method. *Phys. Rev. B* **1998,** *57* (23), 14690-14697.

90. Semin, G. K., On solving secular equations for half-integer spins (I = 5/2, 7/2, and 9/2) in NQR spectroscopy. *Russ. J. Phys. Chem.* **2007,** *81* (1), 38-46.

91. VandeVondele, J.; Krack, M.; Mohamed, F.; Parrinello, M.; Chassaing, T.; Hutter, J., Quickstep: Fast and accurate density functional calculations using a mixed Gaussian and plane waves approach. *Comput. Phys. Commun.* **2005,** *167* (2), 103-128.

92. Lippert, B. G.; Parrinello, J. H.; Michele, A hybrid Gaussian and plane wave density functional scheme. *Mol. Phys.* **1997,** *92* (3), 477-488.

93. VandeVondele, J.; Hutter, J., Gaussian basis sets for accurate calculations on molecular systems in gas and condensed phases. *J. Chem. Phys.* **2007,** *127* (11), 114105.

94. Hartwigsen, C.; Goedecker, S.; Hutter, J., Relativistic separable dual-space Gaussian pseudopotentials from H to Rn. *Phys. rev. B* **1998,** *58* (7), 3641-3662.

95. Genovese, L.; Deutsch, T.; Neelov, A.; Goedecker, S.; Beylkin, G., Efficient solution of Poisson's equation with free boundary conditions. *J. Chem. Phys.* **2006,** *125* (7), 074105.

96. Bussi, G.; Donadio, D.; Parrinello, M., Canonical sampling through velocity rescaling. *J. Chem. Phys.* **2007,** *126* (1), 014101.

97. Wells, H. L., Über die Cäsium- und Kalium-Bleihalogenide. *Z. Anorg. Chem.* **1893,** *3* (1), 195-210.

98. Nazarenko, O.; Yakunin, S.; Morad, V.; Cherniukh, I.; Kovalenko, M. V., Single crystals of caesium formamidinium lead halide perovskites: Solution growth and gamma dosimetry. *Npg Asia Mater.* **2017,** *9*, e373.

99. Dirin, D. N.; Cherniukh, I.; Yakunin, S.; Shynkarenko, Y.; Kovalenko, M. V., Solution-grown $CsPbBr_3$ perovskite single crystals for photon detection. *Chem. Mater.* **2016,** *28* (23), 8470-8474.

100. Krieg, F.; Ochsenbein, S. T.; Yakunin, S.; ten Brinck, S.; Aellen, P.; Süess, A.; Clerc, B.; Guggisberg, D.; Nazarenko, O.; Shynkarenko, Y.; Kumar, S.; Shih, C.-J.; Infante, I.; Kovalenko, M. V., Colloidal $CsPbX_3$ (X = Cl, Br, I) nanocrystals 2.0: Zwitterionic capping ligands for improved durability and stability. *ACS Energy Lett.* **2018,** *3* (3), 641-646.

101. Protesescu, L.; Yakunin, S.; Bodnarchuk, M. I.; Krieg, F.; Caputo, R.; Hendon, C. H.; Yang, R. X.; Walsh, A.; Kovalenko, M. V., Nanocrystals of cesium lead halide perovskites ($CsPbX_3$, X = Cl, Br, and I): Novel optoelectronic materials showing bright emission with wide color gamut. *Nano Lett.* **2015,** *15* (6), 3692-3696.

102. O'Dell, L. A.; Schurko, R. W., QCPMG using adiabatic pulses for faster acquisition of ultra-wideline NMR spectra. *Chem. Phys. Lett.* **2008,** *464* (1), 97-102.